Multi-technique Approach to the Petrophysical Characterization of Berea Sandstone Core Plugs (Cleveland Quarries, USA).

Rikan Kareem, **Pablo Cubillas**, **Jon Gluyas,** Department of Earth Sciences, Durham University, South Road, Durham, DH1 3LE, United Kingdom, **Leon Bowen,** Department of Physic, Durham University, South Road, Durham, DH1 3LE, United Kingdom, **Stephen Hillier**, The James Hutton Institute, Craigiebuckler, Aberdeen AB15 8QH, UK &Department of Soil and Environment, Swedish University of Agricultural Sciences, Box 7014, Uppsala SE-750 07, Sweden, and **H. Christopher Greenwell,** Department of Earth Sciences, Durham University, South Road, Durham, DH1 3LE, United Kingdom

Corresponding author: chris.greenwell@durham.ac.uk

Abstract

Berea sandstone has been used by the petroleum industry as a representative model siliciclastic rock for a number of years. However, only incomplete data has been reported in the literature regarding its petrographic, geochemical, and petrophysical properties. In particular knowledge of the mineral distribution along the pore walls is particularly scarce, despite the fact that mineral exposed in the pore space will be crucial in determining the rock-fluid interactions that occur during core-flooding experiments. In this paper, four Berea sandstone samples (with 4 different permeability ranges from < 50 mD, 50-100 mD. 100-200 mD, and 500-1000 mD) were subjected to a multi-technique characterization with an emphasis on determining the mineral composition, and distribution at the pore surface as well as pore structure and connectivity analysis. The mineral distribution was measured in two-dimensions by chemical mapping using energy dispersive X-ray spectroscopy–scanning electron microscopy (SEM–EDX). The bulk composition of the Berea sandstones was also measured by X-ray diffraction and micro-X-ray computed tomography. From this, it was found that authigenic minerals, especially clay minerals, make up a small portion of the bulk rock volume (3.3% to 8%) but are over-represented at the pore surfaces and in pore spaces compared to the other major mineral constituents of the rock (quartz and feldspar). The effective mineralogy, from the standpoint of rock-fluid interactions, is the mineralogy that predominates at pore surfaces. For the Berea sandstone samples studied, the effective mineralogy is represented, mainly, by kaolinite, illite, and chlorite. For 3 of the four permeability ranges studied, kaolinite is the predominant pore lining mineral observed. In the remaining sample (50-100 mD), illite is the predominant mineral. In addition to SEM, we used atomic force microscopy to show that the nano-sized particles with the shape and size of clay crystals are observed on the surface of recrystallised quartz grains in a Berea sample. Regardless of their origin and identity, the presence of these particles shows that the quartz grain surfaces in Berea sandstone are more heterogeneous than previously assumed. Carbonate cement was somewhat localised throughout two of the Berea sandstone specimens, however, quartz cement is common in all of the Berea cores studied and include both microcrystalline quartz and amorphous silica phases. The pore structure within the four different Berea samples was studied using a combination of X-ray computed tomography, mercury injection porosimetry and high resolution scanning electron microscopy. Results show that two Berea sandstone permeability ranges have a bimodal pore-throat-size distribution whereas the other two were dominated by a unimodal pore-throat size distribution. SEM imaging of the pore network showed that permeability is mainly controlled by pore connectivity in the clay mineral matrix. Next to the pore connectivity, three-dimensional pore space showing both pore-to-pore and pore-to-pore-throat-to-pore relationships are also important.

1. Introduction

In an age of increasing energy use, coupled with the depletion of conventional global oil resources, the development and optimization of enhanced oil recovery (EOR) techniques is critical to sustain oil supplies and to ensure maximum value is delivered from producing oilfield assets. Oil-production from EOR projects continues to supply an increasing percentage of the world's oil. About 3% of the worldwide production now comes from EOR (Aghaeifar et al., 2015). Therefore, the importance of choosing the "best" recovery method becomes increasingly important to petroleum engineers. Low-salinity (LS) water flooding EOR has attracted considerable attention in the last decade due to its potential low-cost as an EOR technique (Tang and Morrow, 1999; Webb et al., 2004; Lager et al., 2006; Sorbie and Collins, 2010). However, despite numerous studies, the main mechanism underpinning increased hydrocarbon recovery by low salinity EOR remains unresolved, particularly in sandstone reservoirs (Strand et al. 2014).

Sandstone reservoirs show the best potential for implementation of EOR projects when compared with other reservoir lithologies and the majority of the pilot and commercial scale studies are in sandstones (Alvardo and Eduardo, 2010). Typically, the heterogeneity of pore-lining minerals in sandstone reservoir rock samples has been postulated to be important in determining underpinning mechanisms during EOR as these have a key role in changing the wettability and modifying fluid flow properties. Use of a standard, model sandstone for test and investigation has been encouraged and the Berea sandstone of eastern Ohio, western Pennsylvania, western West Virginia, and eastern Kentucky has been used extensively in studies of transport mechanisms at the pore scale (denoted hereafter as BST) (Alotaibi et al., 2010; Nasralla et al., 2011b; Zhang et al., 2012). The BST used in the present study is from a single sandstone unit deposited above the Bedford shale formation, representing a cycle of deposition during an oscillation in the land and sea level (at first subaerially as a delta, and later as a marine pavement that formed as the sea inundated this delta) between two periods of tectonic quiescence of the Devonian period (Pashin and Ettensohn, 1995). Previous studies have deployed various high resolution imaging techniques to characterize reservoir sandstones, including scanning electron microscopy (SEM) and micro X-ray computer tomography (μ-XCT), as the basis for statistical models of the volumetric and effective mineralogy distribution within different sandstone samples, including BST (Peters (2009); Bera et al., (2011); Landrot et al., (2012); Golab et al., (2013); Waldmann et al., (2014); and Lai and Krevor (2014)). However, hitherto these studies have not been conclusive in quantifying the amount and distribution of clay minerals in sandstones (and in particular, within the pore space). This is very important, owing to the potential reactivity of clay mineral surfaces with pore fluids. There has also been a substantial discussion of the uncertainties associated with measuring the reactivity of surface-coating minerals (e.g. the importance

of edge surface areas for phyllosilicate clay minerals such as smectites (Metz et al., 2005), or etched surfaces in quartz grains (Gautier et al., 2001).

In this work, pore-lining, reactive minerals, which include minerals other than quartz and K-feldspar (e.g., kaolinite, illite and surface coating nanoparticles), were studied using SEM mineral mapping techniques, and then compared with volumetric mineralogy obtained using X-ray diffraction (XRD) and μ-XCT. Atomic force microscopy (AFM) was used to characterize nanoparticles covering the pore-lining minerals, and therefore, gain a level of understanding unachievable by conventional and even high-resolution SEM imaging. Finally, a study of the pore distribution and connectivity within BST was undertaken using μ-XCT and mercury injection capillary porosimetry (MICP). The overarching goal of this study is to identify inter- and intra-mineral heterogeneity on the pore surfaces of BST to demonstrate the use of a multi-technique/multi-scale approach for rock characterization. Since selected core plugs exhibit macroscopic and nanoscopic heterogeneities associated with changes in the depositional environment and diagenesis, it is beyond the scope of this study to characterise the full range of variability in BST. However, representative samples have been chosen from each of the four permeabilities to study the variations. The information gathered in this study will be used to design future core-scale low salinity EOR studies, where a detailed knowledge of surface mineral reactivity and post-flood changes will be needed.

2. Methods and characterization

In total, twenty six Berea core samples, obtained from Cleveland Quarries, USA, were studied. These samples can be grouped into 4 permeability ranges, referred to BST.1 to BST.4 (Table 1) Four samples of BST.1, five samples of BST.2, thirteen samples of BST.3, and four samples of BST.4 were studied. Details of the characterized properties are presented in Table.1. The core samples chosen for the study were shipped to the UK as drilled to a small 1 ½" diameter x 2" long core from the corner of the quarried blocks which were approximately 7' x 4 ½' x 4' (Darlene Ondercin, personal communication, April 6, 2016).A request was made in order to ensure that bedding plane orientation was parallel to the length of the requested cores.

2.1Bulk composition

2.1.1 Optical microscopy petrographic study. A detailed optical microscopy study on 52 thin sections was performed using a Nikon Eclipse 50iPOL polarizing microscope. Two thin sections from each of the 26 core samples were characterized (Fig. 1A in the Supplementary Information). One thin section was parallel to the length of the BST core plugs (bedding plane orientation), and the other was a plane perpendicular to the length of core plugs. Although these thin sections are susceptible to local heterogeneities in the BST core samples, taken together, two thin sections were taken to be sufficient to adequately represent the main composition of the entire Bulk sample (Fig. 1A in the Supplementary

Information). Standard thin section, included sectioning impregnating with epoxy resin, and polishing was performed for the 26 BST core samples; with a typical thickness of each section ca ~50 μm.

All thin sections were prepared by the thin section service in the Department of Earth Sciences at Durham University. Primarily, optical microscopy informed the selection of samples for additional analysis. The objective of the optical analysis was to quantify the detrital and authigenic mineralogy, texture, and spatial pore distribution. This was accomplished by using the standard point-count technique (300 points per thin section).

Table 1. Petrophysical properties of studied BST core plugs.

Plug No	ID	Permeability	Description		Bulk Volume (cm^3)	Density	Porosity
			Dimeter (mm)	Length (mm)			
1	BST.1	<50 mD	19.2	51.4	14.8	1.0	20.1
2		<50 mD	19.2	51.3	14.8	1.0	19.7
3		<50 mD	19.1	51.3	14.7	1.0	19.9
4		<50 mD	19.1	50.5	14.5	1.0	20.4
5	BST.2	50-100 mD	20.1	50.8	16.0	1.0	20.4
6		50-100 mD	20.1	51.3	16.2	1.0	16.8
7		50-100 mD	20.1	50.9	16.1	1.0	20.8
8		50-100 mD	20.1	51.9	16.4	1.0	20.1
9		50-100 mD	20.1	50.5	16.0	1.0	20.1
10	BST.3	100-200 mD	20.0	50.0	15.7	1.0	20.7
11		100-200 mD	20.1	50.0	15.8	1.0	21.8
12		100-200 mD	20.0	50.0	15.7	1.0	18.1
13		100-200 mD	19.9	50.0	15.5	1.0	22.1
14		100-200 mD	20.0	50.0	15.7	1.0	21.7
15		100-200 mD	20.0	50.0	15.7	1.0	20.0
16		100-200 mD	20.0	50.0	15.7	1.0	17.4
17		100-200 mD	20.0	50.0	15.7	1.0	18.5
18		100-200 mD	20.0	51.1	16.0	1.0	20.5
19		100-200 mD	20.0	51.4	16.1	1.0	21.3
20		100-200 mD	20.0	51.0	16.0	1.0	20.8
21		100-200 mD	20.0	50.7	15.9	1.0	20.0
22		100-200 mD	20.0	51.1	16.0	1.0	20.1
23	BST.4	500-1000 mD	19.8	51.5	15.9	1.0	23.4
24		500-1000 mD	19.9	50.5	15.7	1.0	23.9
25		500-1000 mD	20.0	52.7	16.5	1.0	24.5
26		500-1000 mD	20.0	52.2	16.3	1.0	25.6

2.1.2 X-Ray diffraction - Mineralogical identification. The mineralogical composition of selected samples, one from each of the 4 permeability ranges of BST studied, was obtained via whole-rock X-ray diffraction (XRD) analysis with a full pattern fitting reference intensity ratio (RIR) method, as described in Omotoso et al. (2006), at the James Hutton Institute, Aberdeen. For each of selected cores, a small 1 cm dia x 1cm long piece was drilled perpendicular to the main core length (bedding planes) in order to use the same subsample for XRD and X-ray CT characterisation (Fig. 1A in the

Supplementary Information). For whole rock XRD samples were prepared by McCrone milling followed by spray drying. XRD patterns were recorded on a Bruker D8 Advance from 4-70°2θ, counting for 384 seconds per 0.0194° step, using a Lynxeye XE position sensitive detector and Ni-filtered Cu radiation. The weight percentage of each mineral phase was converted to a volume fraction and grouped into four categories (as discussed below) in order to compare with X-ray CT data for the purpose of determining the volumetric fraction of mineralogy. Details on how this conversion is done can be found in the Supplementary Information. Sample-specific clay mineralogy was also obtained by means of X-ray diffraction (XRD) analysis of the clay mineral fraction separated from the bulk XRD sample, also performed at the James Hutton Institute, Aberdeen. XRD data was collected on a Siemens D5000 instrument using cobalt radiation. Clay fractions of < 2 μm were obtained by timed sedimentation, prepared as oriented mounts onto glass slides using the filter peel transfer technique and scanned from 2 - 45° (2θ) in the air-dried state, after glycolation (vapor pressure overnight), and after heating to 300 °C for one hour. For clay minerals present in amounts > 10 wt. % uncertainty is estimated as better than ± 5 wt. % at the 95% confidence level.

2.2 Scanning electron microscopy. BST samples were analysed for detrital and authigenic mineralogy, porosity and pore connectivity, texture, and mineral distribution through a combination of SEM images of broken samples and backscattered electron (BSE) microscopy with an energy dispersive X-ray (EDX) analysis on thin sections. For determination of the relative percentage of mineral area within BST core samples AZtecEnergy - EDS software was used. The same optical thin sections, oriented parallel to the length of the BST core plugs (bedding plane orientation) were used in the BSE analysis. The thin sections were carbon coated (25 nm) using a Cresington 108 carbon/A (Fig. 1A in the Supplementary Information).The typical thickness of each thin section was ca ~50 μm. Observations of thin sections used a Hitachi SU-70 high-resolution analytical SEM, equipped with an Oxford Instruments energy dispersive X-ray spectroscopy (EDS) microanalysis system (INCA Energy 700), at the G. J. Russell Electron Microscopy Facility, Durham University. BSE imaging of thin sections allowed relative identification of minerals (Dilks and Graham, 1985; Tovey and Krinsley, 1991) within the BST. For each of the 26 thin sections, one set of large-scale images (1 mm by 1 mm) were obtained for large area chemical phase map montage production. For all the images, the locations were assigned randomly. EDS were obtained for mineral phase identification. Phase identification was achieved via offline using Oxford Instruments AZtecEnergy - EDS software, giving the area fraction of each specific mineral.

The mineral phases identified in the BST polished thin sections were divided into several mineral groups: quartz, K-feldspar, plagioclase, muscovite, ankerite, siderite, anatase, chlorite, kaolinite and illite/smectite which correspond with the phases identified directly by XRD (Section 2.1). Measured mineral area fractions were normalized to the “total pore area” within the section to better reflect the

true representation of the mineral within the pore space. The "total pore area" includes the actual empty space in addition to the area occupied by the pore lining minerals (i.e. the space delimited by the detrital grains). The normalized measurements allowed comparison with the µ-XCT data (Section 2.3). BSE images of each BST thin section specimen (3072 × 2304 pixels) were collected at 20 kV acceleration voltage, 4000 nA beam current, 30 µm aperture size and a 15 mm free working distance. For identification of, cementation in the BST polish thin sections, cathode luminescence SEM (SEM-CL) was used. For this purpose, a representative sample was chosen from the studied thin sections to provide detailed information about the type of cement and quartz overgrowths (Milliken and Lauback, 2000). CL images were taken with an accelerating voltage of 15 kV (in contrast to 20 kV for BSE), 8 nA beam current, and 15 mm working distance.

The topography and texture of detrital grains, clay minerals, and pore connectivity were assessed using SEM imaging, in both secondary electron (SE) and backscattered electron (BSE) modes. Three broken samples (ca ~1-1.5 cm2) per core plug were selected for this purpose; the locations were assigned randomly (Fig. 1A in the Supplementary Information). To avoid artifacts arising from sample preparation, this work follows the processes developed by Soeder (1986), where the effects of sample preparation on porosity were critically assessed. The broken specimens were not dried in a dehumidified oven, in order to prevent damage to the internal pore structures as well as clay minerals.

2.3Micro-X-ray computed tomography

2.3.1 Imaging. Tomographs were taken from small cylindrical specimens with dimensions of 10 mm in diameter and 15 mm in height. These were sampled from a representative BST core in the 4 permeability groups (as shown in Fig. 1A in the Supplementary Information).A small sample diameter was chosen so that the specimen fitted in the field of view during high-resolution scans, ensuring the highest quality, so that an exact comparison of the pore space can be validated with porosimetry analysis. Tomograms were obtained and processed using a Zeiss XRadia-410 CT scanner. The X-ray source was set to 80 kV and 140 µA, a Bremsstrahlung filter was used to enhance the performance of the detector for the X-ray photons to acquire 3201 projections of 2048 pixel^2 over 24 hours. The projection set covered a *ca* 1 mm^3 cube at the center of the studied BST specimen, scanning about the midpoint to minimize the long scan time producing motion artifacts. The projections were reconstructed to a 3-dimensional (3D) raw tomogram, with a voxel size of 1.03 µm/voxel resolution. Tomogram data was processed with Avizo™ 9, a commercially available software package from FEI, to identify surface and pore mineral phases (Buchwalter et al. 2015). Further details of the data processing method are included in the Supplementary Information.

2.3.2 Image processing. In a tomographic image, the value of each volume voxel represents the average X-ray attenuation property of that material in that specific volume. The degree of attenuation

depends on the elemental composition and bulk density of the material. This gives the technique the potential for mineral phase identification. In recent years, image acquisition methods applied in mineral identification derived from X-ray CT scanning have improved considerably as shown by Peter (2009), Landrot et al. (2012), Golab et al. (2013), Hezel et al (2013), and Lai et al (2015). In this work, BST specimen data were resolved from artifacts using a non-local mean filter (Buadeseta et al. 2005). Once the noise had been reduced to an adequate level, in Avizo™ 9, watershed segmentation was applied for both binary and multiphase segmentation. Segmentation is a procedure by which the grayscale data is transformed into binary data required for quantitative analyses. During setting of gray scale thresholds, special focus was set on the conservation and representation of grain and pore boundaries, which were selected manually. The specific parameters, such as the gray intensity range for each mineral group used per BST specimen, are provided in the Supplementary Information. The solid phase of the BST specimens was further segmented into mineral groups using a similar approach to that reported by Golab et al. (2013) and Lai et al. (2015). Table 2 summarises the definition of the segmentation groups used for the BST specimens. The quartz group consisted of only quartz. The feldspar group consists of feldspars plus muscovite since it has a similar attenuation to feldspars. Kaolinite, illite/smectite, and chlorite comprised the clay mineral group. Calcite, ankerite and siderite, and remaining oxides such as anatase, formed the last group (other).

Group name	Major Mineral	Minor Mineral
Quartz	Quartz	
Feldspar	alkali feldspar	plagioclase, albite, and muscovite
Clay	Kaolinite	illite, and chlorite
Other	Ankerite	siderite, calcite, and anatase

Table 2. Description of the X-ray segmentation groups for the Berea sandstone.

For each of 8 scanned samples from the 4 BST groups, we selected several representative subvolumes and characterised their porosity, pore size distribution, and pore volume in order to increase efficiency of computation. The size of those subvolumes ranged from 4000×4000×4000 μm^3 to 1000 × 1000 ×1000 μm^3. The higher the atomic number or density, the more X-rays are absorbed, creating darker regions in the tomograph (Cnudde, 2009). After implementing segmentation manually, a "hole filling" function in Avizo™ 9 was employed on the data so that any isolated black voxels (isolated holes within minerals) were converted into white voxels (i.e. counted as solid matrix). The solid matrix was removed and the pore space converted into a pseudo-solid matrix and quantified. The number of pores and their volume distribution was computed for all BST core samples (Houston et al. 2013). A similar approach was implemented to quantify detrital grains and their distribution in the scanned BST specimens.

2.4 Atomic force microscopy (AFM) characterization. A multimode Bruker AFM, equipped with a Bruker Nanoscope V controller, was used to characterize the surface of selected BST mineral grains exposed in the core pores. A representative section of a BST.4 core specimen was cut using a low speed saw to produce a sample of 10mm × 10mm × 1mm dimensions. The specimen was studied using SEM to identify an adequate area to scan with the AFM. Flat crystal surfaces with an orientation approximately parallel to the sample holder surface were used and were placed in a gold sputtering apparatus, and covered with a small foil disk with a 20 μm aperture in the center. A small gold reference mark was created on the center of the sample to locate the same area scanned on the SEM with the optical microscope attached to the AFM. SEM images at different magnifications were collected so a length scale similar to images produced by the optical microscope (attached to the AFM) could be easily obtained and then allow comparison. Special emphasis was placed on areas that showed well developed (therefore flat) quartz surfaces from selected samples to scan using the AFM. All scans were performed using PeakForce™ tapping mode and scanasyst-air probes (Bruker probes). Image analysis was carried using Nanoscope Analysis version 1.5 (Bruker).

2.5. Mercury injection porosimetry. Mercury Injection Capillary Porosimeter (MICP) is a method used for characterizing the distribution of pore throat structure (Hildenbrand & Urai, 2003; Yven et al., 2007) in a porous material. The method is based on the fact that a non-wetting liquid can intrude the pore space when pressure is sufficiently high: the higher the pressure, the smaller the pore throats that are filled with mercury (Abell et al., 1998). By using the Washburn equation (Washburn, 1921), the pressure differences can be converted to pore access diameters, assuming that the porous material consists of a bundle of nonintersecting tubes (Howard, 1991). Based on a set of assumptions on pore morphology, a pore throat size distribution curve is obtained from the intruded volume at each pressure step. The samples used in this analysis were first scanned using X-ray CT, and after this, they were analysed using MIP. Mercury injection on smaller core plugs (1cm in diameter and 1.5cm long) drilled out of the representative of BST core samples (Fig. 1A in the Supplementary Information). Ideally, a sample analysed by MICP should be as large as possible. However, a small sample diameter was chosen so that an exact comparison of the pore space can be validated with μ-XCT analysis. The samples were placed in the mercury filled sample cup in a pressure vessel at the School of Civil Engineering and Geosciences, at the University of Newcastle. Then the pressure was slowly increased from 3 psi to 39,000 psi.

3. Results and Discussion

3.1 Berea sandstone and bulk composition.

The Upper BST unit at the Cleveland Quarries locality, from which the cores in this study originate, is a fine to medium grain size, well-sorted sandstone with closely spaced planar bedding (Churcher et al. 1991). The two main components of BST are detrital grains, such as quartz, alkali feldspar, and plagioclase, and a matrix composed mostly of clay minerals, such as kaolinite and illite/smectite (Pepper, 1944; Lai et al. 2015).

3.1.1 Detrital grains. Observations made with transmitted light plane-polarized and in bright-field reflected light on BST thin sections allowed the identification of the percent value of framework grains. Modal analysis results for the average 52 studied thin sections (i.e., two thin sections from each of the 26 BST core samples) are presented in Table 3 and Table 1A in the Supplementary Information. In terms of mineralogical composition, the detrital grains can be divided into quartz (Q), feldspar (F) and lithic fragments (L).

Table 3. Averages of multiple thin section data set from BST core samples showing quartz as the main component with their size distribution from selected samples.The range of uncertainty is about ± 15% as three parameters have used in the analysis.Q = Quartz, F = Feldspar, L = Lithic fragments, % QFL=Percent value of framework grains in each sample, and Eq = Equivalent.

Sample No.	Composition			EqDiameter XCT (µm)		
	%Qtz	%F	%L	Minimum	Maximum	Mean
BST.1	83	8	9	13.1	330.6	172.0
BST.2	85	7	8	15.4	284.0	149.8
BST.3	84	8	8	13.2	347.5	184.5
BST.4	91	1	7	13.2	416.6	215.1

SEM images showing details of each mineral component are given in Fig.1. Quartz is represented mainly as monocrystalline grains (Fig. 1a and 1b) and feldspar as K-feldspar with negligible amounts of mica (Fig.1b). Additionally, most of the observed K-feldspar grains in BST show signs of partial to almost total dissolution (honeycombed grains), leading to increased surface area when compared to undissolved grains (Fig. 1c and 1d). The total K-feldspar content of sandstones decreases due to diagenetic processes leading to the formation of intra-granular kaolinite and illite (Bjorlykke 1998). Significant amounts of kaolinite and illite clay minerals arising from the dissolution of feldspar cover large areas of most of the quartz detrital grains (Figs. 1a, 1e, and 1f). Different types of rock fragments, including igneous and sedimentary, are present in the studied samples. Microquartz grains, with an average abundance of 2%, are the most abundant lithic components. Sedimentary rock fragments, averaging 7 %, are mostly composed of authigenic clays.

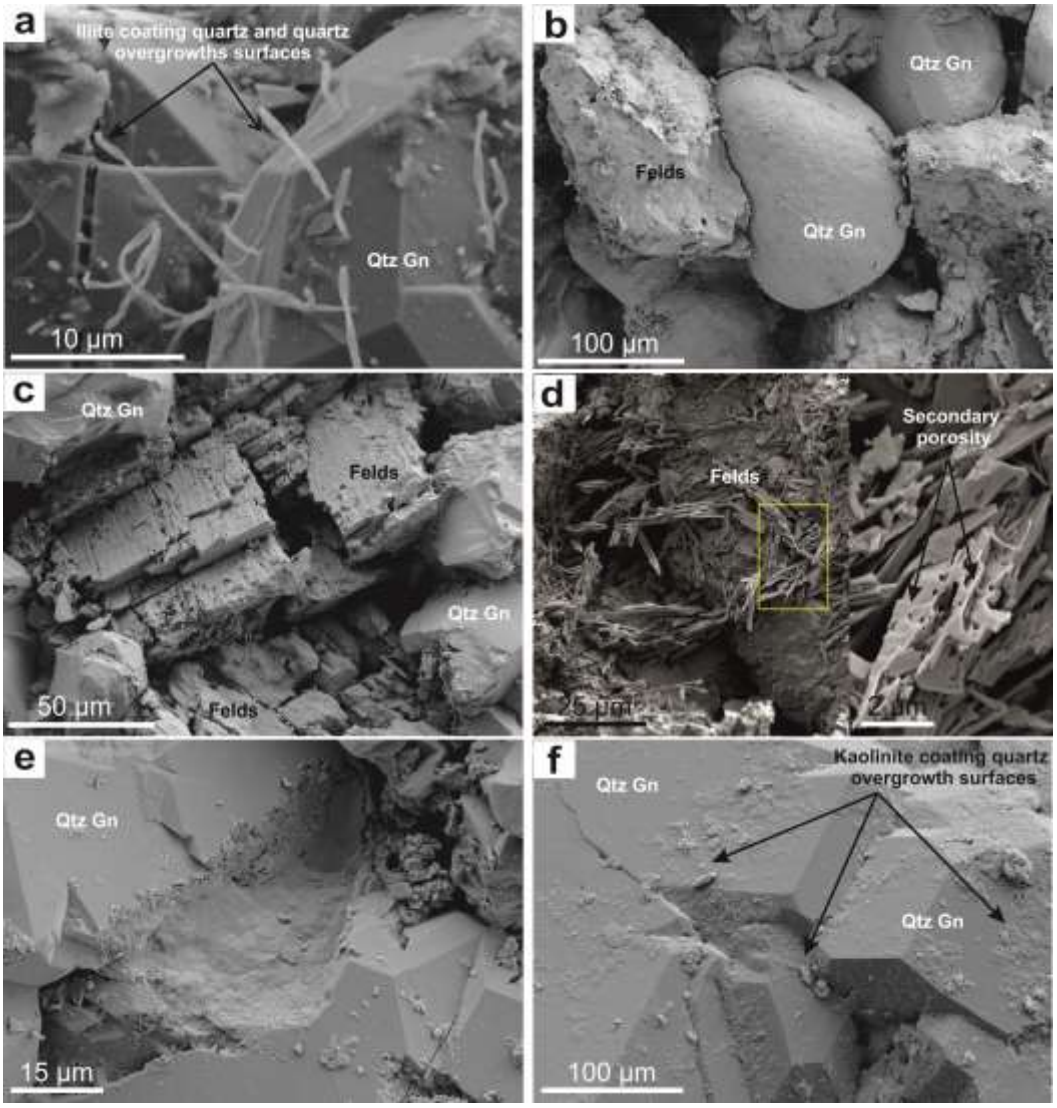

Figure 1. SEM micrographs of BST detrital grains, a) Detrital quartz grains in BST.1 coated by diagenetic clay minerals (hairy authigenic illite) and quartz overgrowths. b) Example of well-rounded quartz crystal from sample BST.4 (classified as a mature quartz arenite). Visible as well are several feldspar grains, showing clear signs of dissolution, and authigenic clay fractions interspersed within the quartz grains. c) Detailed view of detrital K-feldspar grains that are partially dissolved (creating secondary intergranular porosity); in contrast quartz detrital grains show no signs of dissolution. d) Detailed view of secondary porosity in a dissolved K-feldspar grain in BST.2 which is surrounded by detrital quartz grains and kaolinite crystals generated by extensive dissolution of detrital K-feldspar grain during diagenesis. Although this type of dissolution clearly creates intragranular pores, without further dissolution of other phases, such pores can remain largely unconnected, and thus may not significantly affect permeability. e) Quartz overgrowth in BST.4. In addition a layer of kaolinite over growth is visible covering part of the quartz crystals. f) Well-formed quartz overgrowths in BST.4. The growth of a thin clay coating (probably kaolinite), as seen here, would ultimately help to prevent further cementation. Qtz = quartz and Felds = feldspar.

arenites (Fig 2a). The result of the equivalent grain diameter analysis (conducted using the µ-XCT data) of all BST specimens show a wide range of grain sizes from coarse (240 µm) to very fine (13 µm) (Fig. 2). The average equivalent diameter of the detrital grains in the cores of BST.1 and BST.3

groups are relatively close to each other, with values of 171 μm and 184 μm, respectively (Figs. 2b and 2d), as reported in Table 3. Based on frequency distribution (Fig. 2c), the average equivalent diameter for BST.2 is smaller (149 μm) than that of BST.1 and BST.3, whereas the average equivalent diameter for BST.4 is the largest, at 215 μm (Fig. 2e). From quantitative XRD analysis, the volume fraction of quartz is similar for samples BST.1, BST.2 and BST.3 (just above 80%). However, for sample BST.4 the volume of detrital quartz grains is 95.05% of the bulk volume. Notably, the segmented quartz volume values calculated from the μ-XCT data show excellent agreement with the total volume fraction of quartz minerals measured using XRD (Table 4).

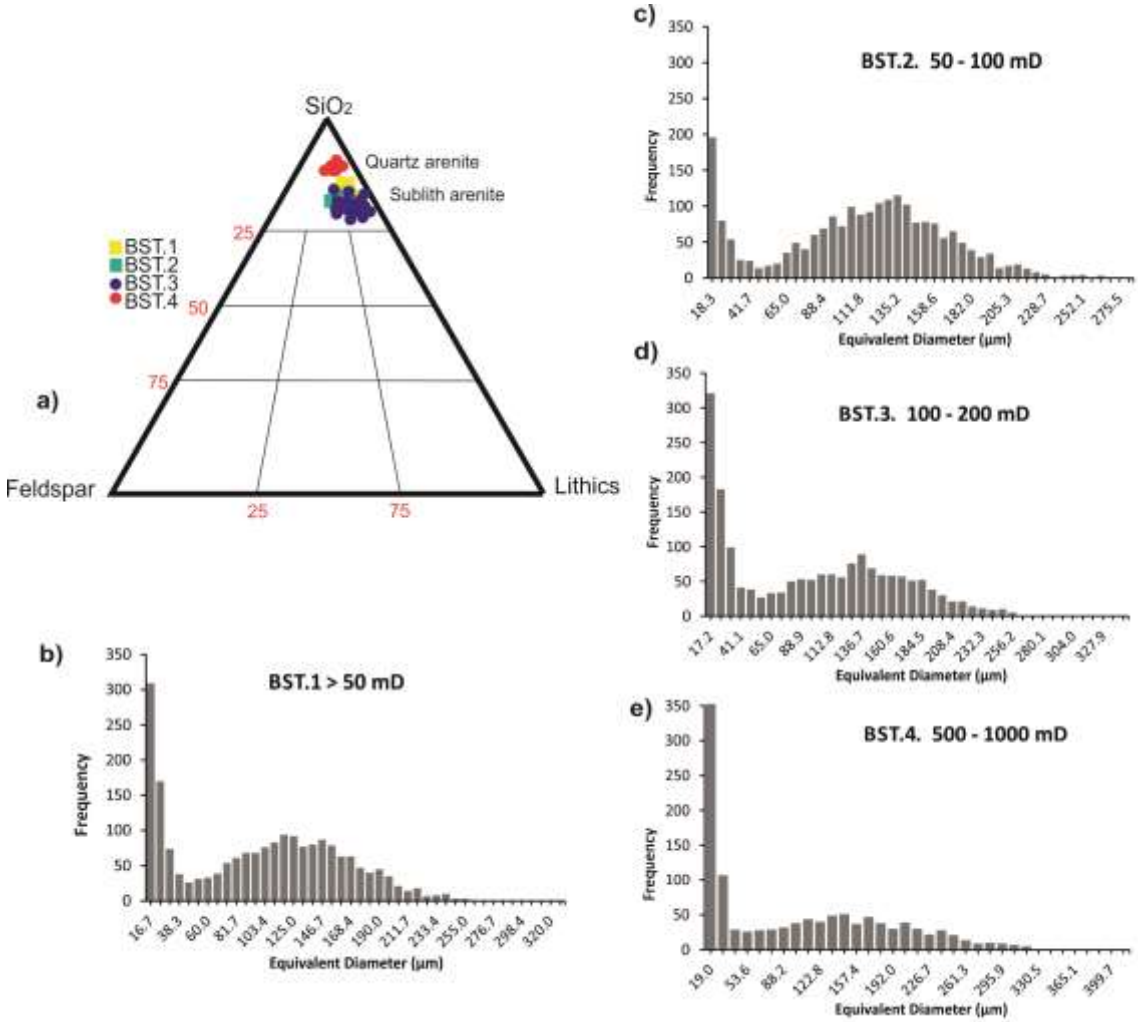

Figure 2. a) Ternary diagram showing the framework composition (based on the classification of Folk (1980)) for the 4 BST samples studied. BST.1, BST.2, and BST.3 are classified as litharenites, and BST.4 as a quartz arenite. Grain size distribution plots obtained from μ-XCT data for: b) BST.1, c) BST.2, d) BST.3, and e) BST.4.

Table 4. Mineral volume fraction and area fraction for all BST core sample from XRD, X-ray CT, and SEM/EDX.

Sample ID	Group	Wt% from XRD	Volume fraction		Area fraction
			XRD	XCT	SEM
BST.1	Quartz	81.5	81.9	83.7	61.1
	Feldspar	6.5	6.6	6.2	7.0
	Clay	8.2	8.0	9.1	16.7
	Other	3.7	3.4	0.9	15.1
		99.9	99.9	99.9	99.9
BST.2	Quartz	84.5	84.9	83.8	76.2
	Feldspar	5.8	5.8	6.9	8.3
	Clay	6.8	6.7	7.8	11.7
	Other	2.8	2.5	1.4	3.7
		99.9	99.9	99.9	99.9
BST.3	Quartz	82.7	83.1	82.9	75.0
	Feldspar	7.0	7.0	6.9	4.0
	Clay	7.1	6.9	8.4	14.4
	Other	3.1	2.7	1.7	6.5
		99.9	99.7	99.9	99.9
BST.4	Quartz	95.1	95.3	94.9	95.1
	Feldspar	0.8	0.8	1.1	0.0
	Clay	3.4	3.3	3.6	4.6
	Other	0.6	0.5	0.3	0.2
		99.9	99.9	99.9	99.9

Based on quantitative XRD analysis, the volume fraction of K-feldspar is similar for samples in the BST.1, BST.2 and BST.3 (around 4% to 5%) groups. However, for samples in the BST.4 group, the volume of K-feldspar grains is less than 1% of the bulk volume. Remarkably, the total volume fraction of K-feldspar minerals measured using XRD (Table 4) matches with values obtained from the point counting method as can be seen in Table 3 and Table 1A (in the Supplementary Information). In addition, the BSE phase maps (Fig.3) collected at 1000 μm^2 shows that the area of feldspar fraction appears to be higher in 3 of the 4 BST permeability groups. It is clear the total K-feldspar content decreased with an increasing permeability range. The area fractions of minerals (measured from the SEM mineral phase mapping) are shown in Table 4. The partial dissolution of detrital feldspar grains across all samples is a common feature and leads to an increasing exposed area in comparison to other detrital grains (Figs. 1c and 1d). In fact, different dissolution stages, from partial to complete dissolution, can be seen across the BST core plugs. Moreover, the dissolution of detrital feldspar grains would mean a large exposed area of the mineral to any pore fluids e.g. injected low salinity brine. From this, it is clear the physico-chemical properties of the brine water/rock interactions depend on the accessibility and type of minerals in contact to the open pore system.

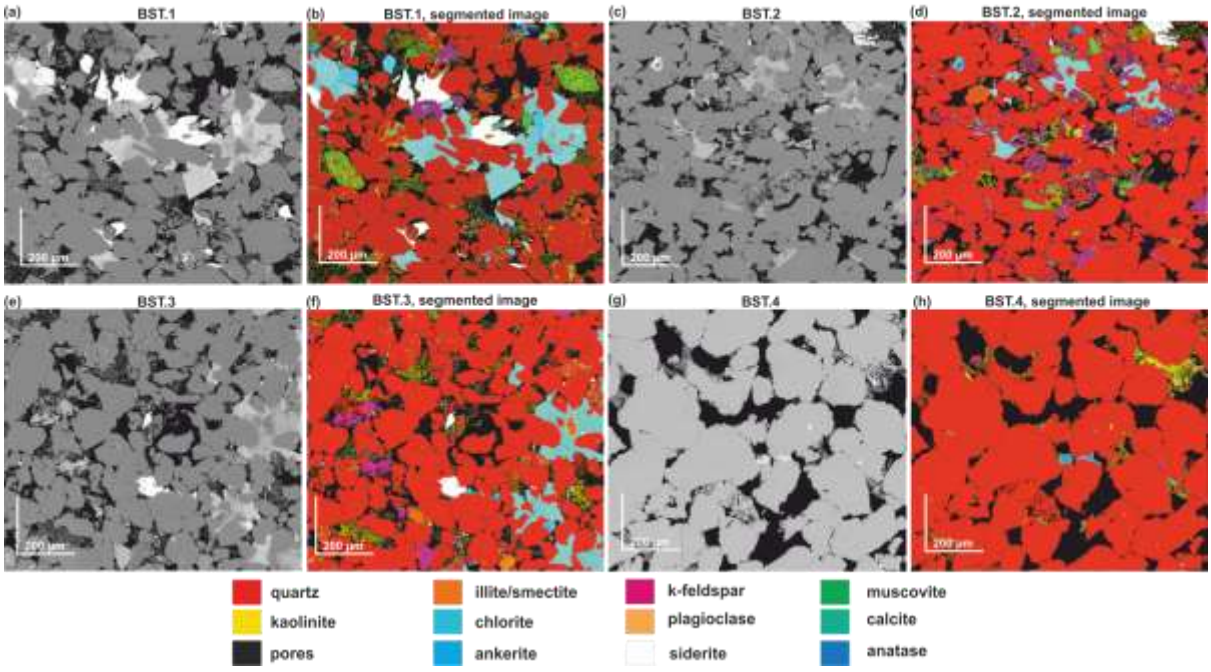

Figure 3. BSE and corresponding phase mapping images of BST.1 (a and b), BST.2. (c and d), BST.3 (e and f), and BST.4 (g and h). The analytical conditions were: beam intensity of 20 kV. Image interpretation data are shown in Table 4.

3.1.2 Matrix (detrital and authigenic minerals). Previous work on BST, based on SEM imaging, has shown that detrital grains are mainly cemented by authigenic minerals such as kaolinite, illite, and chlorite (Churcher et al. 1991). Although authigenic clay minerals are undoubtedly present in both the matrix and intergranular pore spaces, it can be difficult to distinguish authigenic clays from detrital clays either by petrography or by standard crystallographic techniques e.g. optical microscopy and X-ray diffraction (XRD). In addition, complex micro-textural and micro-chemical relationships (Hurst 1999) and low abundance complicate the use of many geochemical methods in characterizing clay minerals in reservoir sandstones. For the purpose of determining the matrix mineralogical composition, whole rock, and clay separate (< 2 μm) XRD analysis of a representative sample of each BST core plugs was performed. Results from these analyses are shown in Fig.4a and 4b. From the XRD patterns, well-ordered kaolinite was identified (with a *d*-spacing of ca. 7.15 Å). SEM images corroborate this finding, as seen in Fig. 6d, which shows large, well-formed, kaolinite crystals. Some of the more blocky forms are reminiscent of the habit often adopted by dickite, but close inspection of the random powder diffraction data failed to identify any dickite in the samples, only kaolinite was identified. Both illite and illite/smectite, the latter with about 15% expandable (smectite) layers, were identified as distinct minerals from the measured 10 Å spacing in the XRD patterns, and from the broad 'tails' to the 10 Å peak that change in response to glycolation and heating (Fig. 4b). From SEM observations, however, it can be observed that most of the illite identified from XRD is detrital and is clearly incorporated in the clay matrix (Fig.6). Small amounts (< 1%) of discrete chlorite (*d*-spacing:

14 Å) also occur in all the BST core samples (Table 1B in the Supplementary Information). In addition, during heating BST samples to 300 °C, for one hour, the chlorite shows some sensitivity which is often indicative of iron-rich chlorite possibly with berthierine interstratification (Fig. 4b).

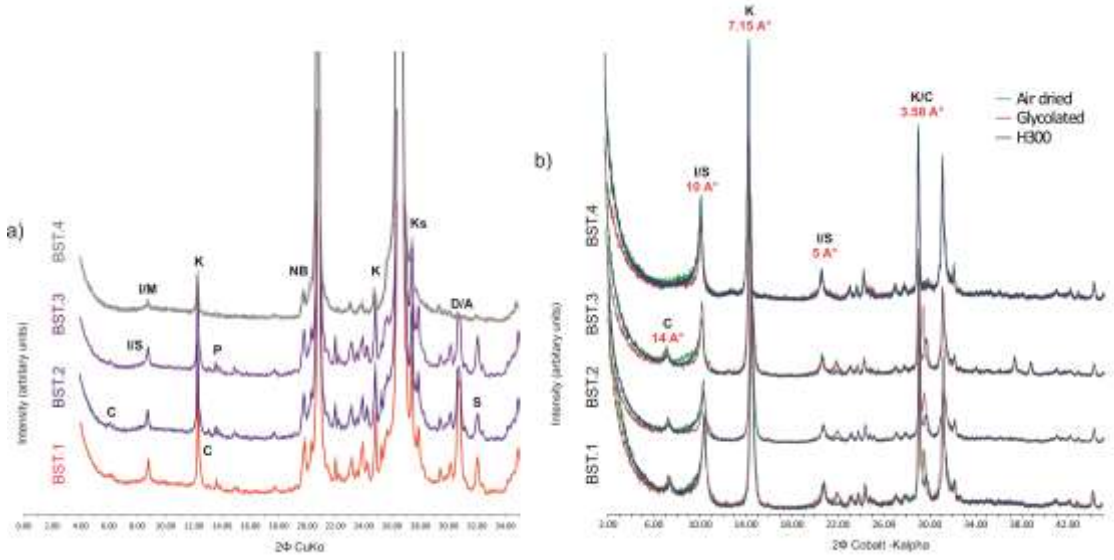

Figure 4. XRD patterns of all BST core samples. a) Whole-rock XRD patterns. Patterns are offset for clarity and main quartz peaks are off scale to show detail of other minerals present .b) XRD patterns from the clay fraction (2 < µm). The main peaks in the patterns are kaolinite, illite, illite/smectite, and chlorite; several other trace minerals (not labelled) are also present. I/M = Illite/mica, I/S = Illite/smectite, K = Kaolinite, C= Chlorite, P = Plagioclase, NB = non-basal clay Ks= K-feldspar, D/A = Dolomite/Ankerite, S = Siderite.

BSE/EDX images of the BST core samples, respectively. The results for estimating the area fraction are listed in Appendix C of the Supplemental Information section. The area fractions of kaolinite in BST.1, BST.2, BST.3, and BST.4 are 13.9%, 5.8%, 5.2%, 3.1%, respectively. For illite, the area fraction for the 4 BST groups is 2.1%, 6.0%, 2.7, and 1.6%, respectively. In comparison to illite, kaolinite shows a higher area fraction for samples BST.1, BST.3, and BST.4. In contrast, when compared with kaolinite in BST.2, illite crystals occupy most of the total pore space (Fig. 2c in the Supplementary Information). These differences in area fraction have implications for the BST quality parameters (e.g. porosity, permeability), as will be discussed below. According to SEM observations, kaolinite from BST scanned sections are widely dispersed throughout the pore structure in the form of pseudo-hexagonal (Figs. 6a and 6b), and sub-idiomorphic platy crystals loosely attached to pores walls (Figs. 6c and 6d). Kaolinite crystals occupy most of the "total" pore space and therefore are also more exposed to the "open" pore space (Fig. 6c) than the other clay types. Based on the work of Soeder (1986), BST kaolinite crystals, such as those shown in Fig. 6d, do not appear to have experienced significant damage during the sample preparation process. This suggests that the observed clay mineral geometry within BST pore spaces and observed SEM-scale pore connectivity relationships reflect the native rock conditions. In addition, the kaolinite agglomerates show a high

degree of internal porosity, either in the "booklet" form (Figs. 6a, 6c and 6d) or of those composed of more disaggregated crystals (Fig. 6d). These two characteristics (over exposure in the pore system and additional intricate porosity) mean that most of the pore fluid in these BST core samples will be predominantly in contact with the kaolinite and this may have important implications for EOR (it has been shown, clay mineral-oil interactions can affect the wettability of a rock) where Berea sandstone is used as model cores. For example, Lbedeva et al. (2010) and Fogden and Lebedeva (2011) showed that oil adhesion to kaolinite decreases at low brine salinity or pH. This shows that the distribution of clay minerals such as kaolinite has a significant effect on the sandstone rock wettability behavior during oil recovery.

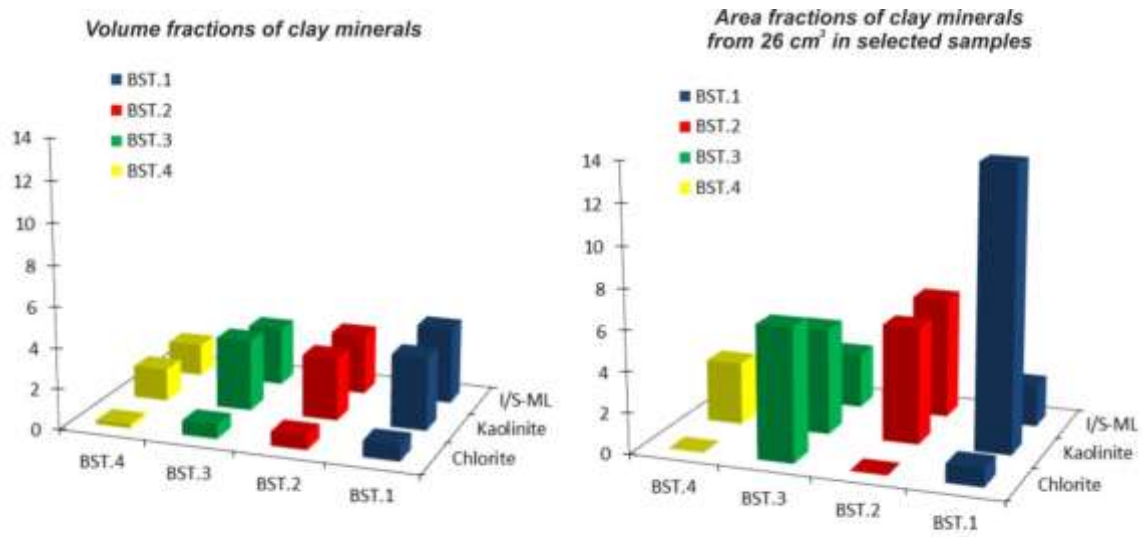

Figure 5. Volume fractions (%) and area fractions (%) of the main clay minerals present in each BST sample obtained from XRD and EDX data, respectively. These data are taken (Tables 1B and 1C in the Supplementary Information).

In comparison, illite crystals are less represented in the open pores across the scanned area of BST core samples, with the exception of the BST.2 samples (Fig 3 and Fig. 2c in the Supplementary Information), but they can also exhibit a great variation of morphologies and internal porosity, which may also lead them to play a role in determining the overall wettability of BST (Figs. 6e and 6f). Based on SEM observation, the majority of illite identified from X-ray diffraction is of assumed detrital origin and is associated with the matrix (Fig. 6). Only in a few cases was authigenic illite identified by SEM (Fig. 6f) (Balthazar, 1991). Finally, the presence of large kaolinite crystals could have a significant impact on reducing intergranular pore volume (Wilson & Pittman, 1977), but more importantly, can act as migrating fines in the pore system (Neasham, 1977). Based on SEM observations, kaolinite crystals can be up to 50 µm thick along the *c axis* and may have a major impact in terms of pore obstruction during waterflooding studies, especially on those BST samples with lower permeability (and smaller pore throat sizes). Although fines migration has been discussed

as a potential mechanism for EOR (Morrow et al., 1999), in the case of BST it may, in fact, hamper oil recovery. Chlorite is the third most prevalent clay in the studied BST core samples (See Supporting Information).

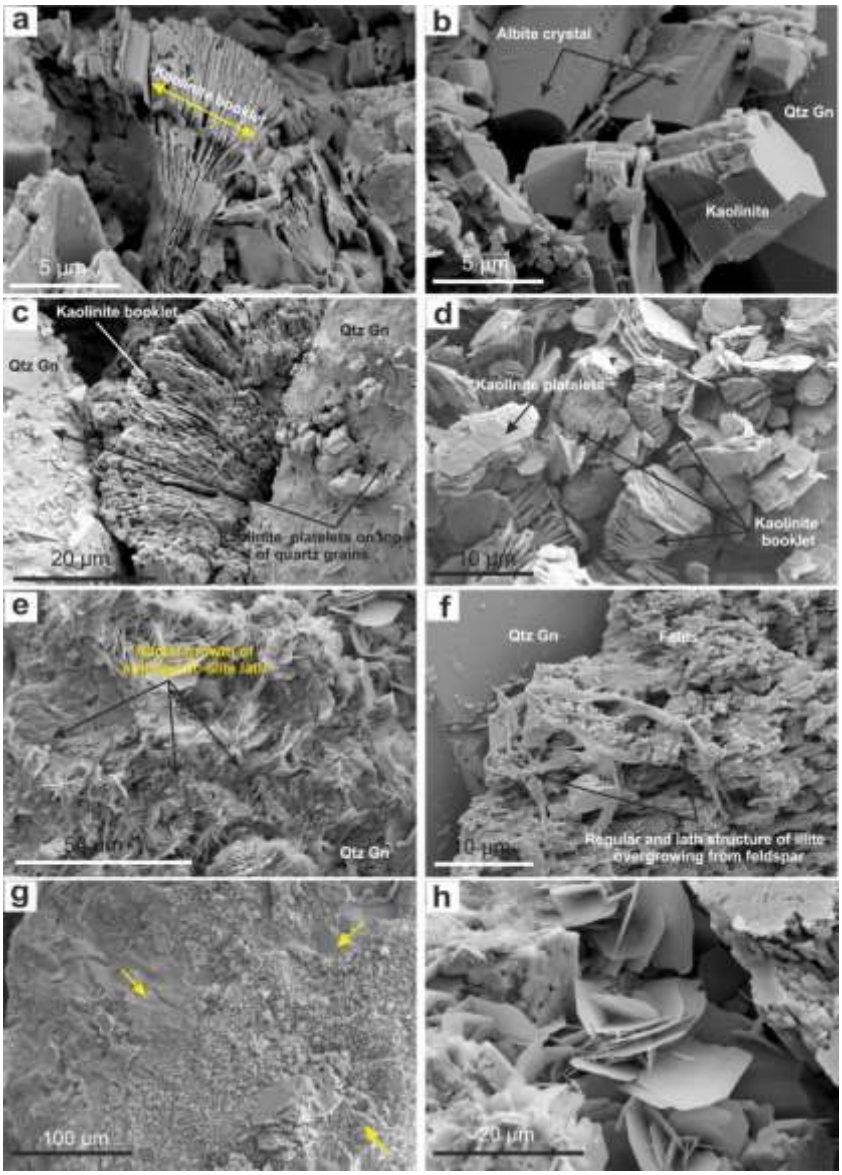

Figure 6. SEM micrographs of the clay matrix in BST samples. a) Detail of kaolinite coatings in BST.3. A well-developed kaolinite "booklet" can be clearly seen. b) Kaolinite crystals in contact with a prismatic, albite feldspar, and a larger detrital quartz grain in BST.4. c) Pore-filling, authigenic kaolinite in BST.3 showing booklet morphology. Smaller kaolinite crystals can also be seen covering the detrital quartz grain. d) Aggregates kaolinite booklets and platelets in BST.4. The plates consist of euhedral, subhexagonal crystal, which display high degree of elongation along the a- or b-axis direction. e) Detailed view of illite crystals with hairy-like morphology in BST.2 Formation of these clay crystals postdates quartz overgrowths. f) Illite crystals growing from a highly dissolved K-feldspar grain in BST.2.g) Chlorite rich region showing intimately mixed between chlorite and another clay mineral in BST.1 (yellow arrows). h) Enlargement area in (g) showing chlorite crystals. Qtz = quartz.

Based on the paragenetic sequence of the Berea reservoir sandstones, the chlorite in BST core plugs is mostly diagenetic in origin (Balthazar, 1991). SEM imaging indicates that chlorite crystallites comprising the detrital grain coatings are generally well crystallized and show a preferred orientation with respect to the substrate (Fig. 6h). Although in BST.3 samples the amount of chlorite is less than 1 vol. %, it has a large area fraction when compared to other authigenic clay minerals including kaolinite and illite (Table 1B in the Supplementary Information). Chlorite is frequently responsible for the preservation of porosity in sandstones rocks (Zhang et al. 2015). However, chlorite in BST core samples is dominantly observed as a pore-lining material and rarely is found to be pore filling (Balthazar, 1991). Finally, the volumetric distribution of each mineral group in selected BST core samples was rendered using μ-XCT (Fig. 7). The volumes shown in the figures represent a sample size of 400 μm × 400 μm × 400 μm. It can be seen that the extent of clay mineral distribution across the whole volume of the sample is relatively even (see Table 1B for XRD mineral volume fractions and Table 1B for BSE mineral area fractions in the Supplementary Information section).

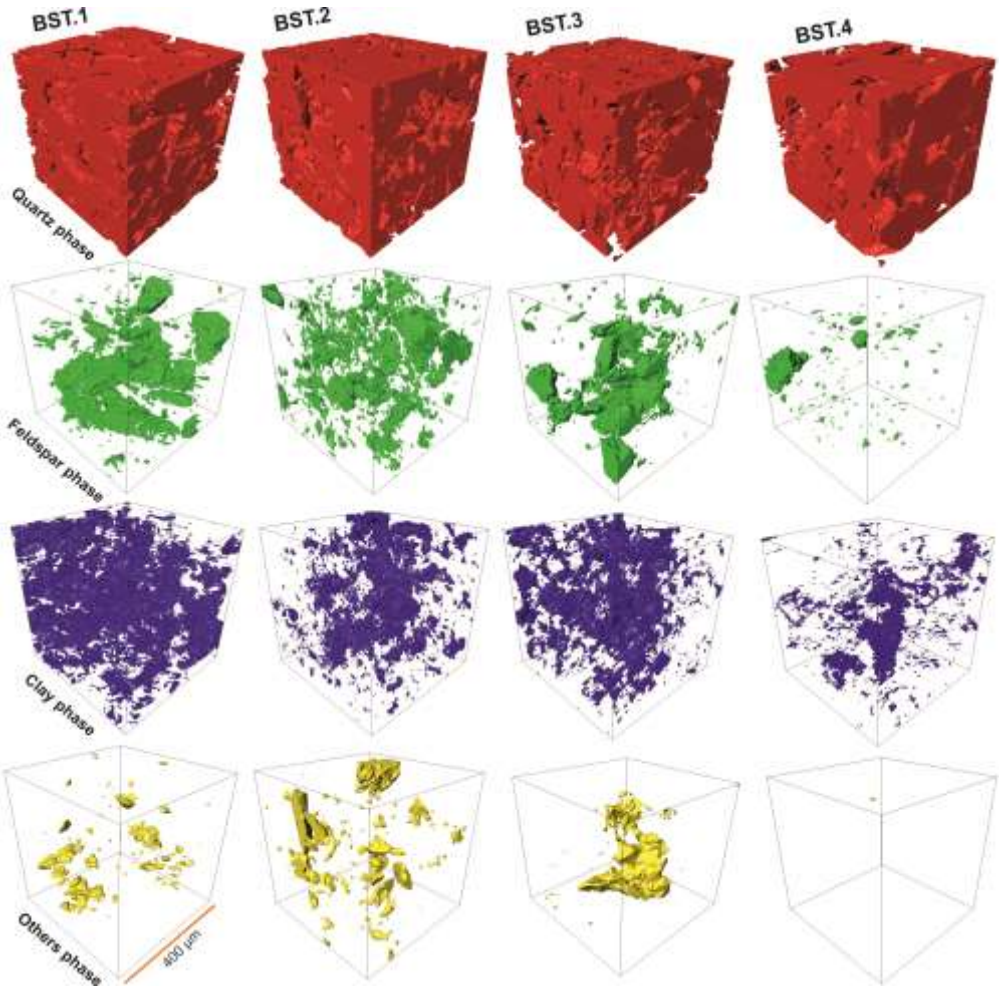

Figure 7. 3-D renderings showing the volumetric distribution of each mineral phase for all BST samples. From top to bottom: Quartz, feldspar, clay minerals, and others (primarily carbonates and oxide)

3.1.3 Cementation. Quartz, ankerite, and siderite are the commonest (non-clay) cement observed in the cores examined in this study as determined by SEM-CL and XRD (Fig 8.Also see Tables 1B and 1C in the Supplementary Information section). Ankerite and siderite commonly exhibit a blocky habit and commonly occlude large portions of intergranular pore space (Figs. 8a and 8b). Ankerite and siderite cement also occlude secondary pores formed after feldspar dissolution (Figs. 8a and 8b).Thin section analysis reveals two generations of ankerite cement characterized by differing amounts of Fe and Mn. In all samples the amount of siderite (e.g., Fig 8a) ranges between 0.1 vol. % and 0.8 vol. %, whereas the amount of ankerite (e.g., Fig. 8b) ranges between 0.1 vol. % and 1-6 vol. % (Table A.1). In addition, it is clear from SEM images (Fig. 3, Fig. 8) that ankerite and siderite have an impact on porosity reduction and may also impact on permeability reduction in the BST core samples, depending on how these carbonate phases are distributed within a pore system.

Two types of quartz cement were identified in BST based on CL images: (1) thick macro-quartz overgrowths and, (2) thin micro-quartz grain coatings. Quartz cement is a volumetrically minor phase ($\leq$ 4 %, Table 1A and 2A in the Supplementary Information) and occludes the pore space in the most of the BST cores studied (Figs.8c and 8d). It is likely, however, that even a small volume of quartz cement would be sufficient to block a number of the pore spaces.

The term "macro-quartz overgrowth" is here used to describe syntaxial quartz overgrowths larger than 20 µm which can be observed between the detrital quartz grains and micro-quartz crystals ranging from 1 µm to 5 µm in optical continuity with detrital quartz grains, as can be seen in (Fig.8e). Quartz overgrowths are most common in the BST.4 samples (3.4%) and BST.3 samples (2.3%), though rare in BST.2 samples and BST.1 samples (1.4%, and 1.1% respectively) as can be seen in Table 1A in the Supplementary Information. The decreased abundance of quartz cement in BST.1 and BST.2 samples is attributed to the early occlusion of pore space. SEM-CL shows that most of the detrital quartz grains have overgrowths, with the thickest being between 50 µm and 100 µm and usually present over monocrystalline, rounded to well-rounded quartz grains, as seen in (Figs. 8f and 8g). Figs 8h and 8i also illustrate that some of the more frequently observed quartz cement are an early generation, which is located as syntaxial overgrowth on detrital grains. Based on a previous investigation on amorphous silica in sandstone rock, these syntaxial overgrowths on quartz grain surfaces in BST are possibly amorphous silica (Worden et al. 2012). Single microquartz crystals (< 5 µm) could be found in between the kaolinite crystals (Fig. 8j).

3.3 Possible nano-scale minerals on mineral surfaces. It has been documented that nano-scale particles, including possible clay minerals and organic coatings, can be present at sandstone pore surfaces (e.g., Hassenkam et. al., 2011, Matthiesen et al., 2014). Furthermore, the aforementioned studies discuss the potential role nanoparticles may play in EOR processes. To confirm the presence of nanoscale surface bound particles in the studied BST core samples, high-resolution SEM imaging

of uncoated samples and atomic force microscopy (AFM) was used to study the exposed surfaces of quartz, feldspar and kaolinite crystals.

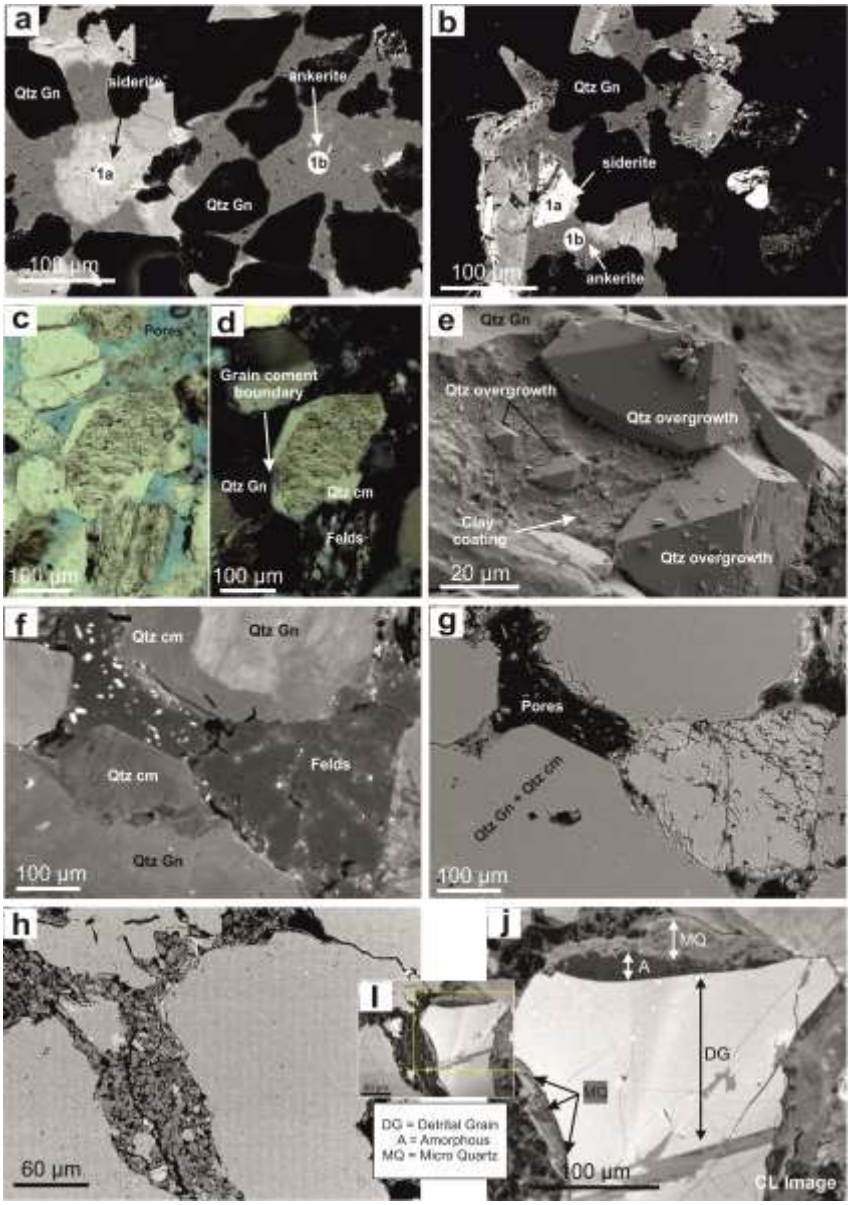

Figure 8. Representative photomicrographs showing porosity loss due to cementation. a) BSE image of detrital quartz grains surrounded by two generation of carbonate cement siderite (1a) and ankerite (1b) in BST.1. b) The same carbonate cement shown in (a) is blocking most of the pore spaces between detrital quartz grains in BST.2 c) Plane polarized image showing quartz cements occluding pores between the coarse detrital quartz grains in the BST.3. Optical micrograph (d), of the same area as shown in (c), shows the grain cement boundary (see white arrow). e) Secondary electron micrograph (BST.2) shows large, euhedral quart overgrowth (cement) filling a pore. Note the detrital grain had early, partial clay coating (see white arrow). f) SEM micrograph shows the advance stage of quartz overgrowth cementation in which a significant amount of primary pore space was filled. SEM-CL micrograph (g) of the same area shown in (f). BSE image (h) reveals that the grains and cements (BST.3) are composed of silica and SEM-CL images, (i) and (j), show isopachous layers of quartz cement, high resolution CL (j) distinguishes the detrital grain with bright luminescence (DG) from the dark amorphous silica layer dark or non-luminescing band (A), and the bright microcrystalline quartz (MQ). Qtz = quartz, cm = cement, Gn= grain, and Felds= feldspar.

3.3.1 Quartz, feldspar, and anatase surface characteristics. As mentioned above, by volume, BST is dominated by detrital grains such as quartz and K-feldspar and based on SEM image analysis these are mostly covered by authigenic minerals such as kaolinite, illite, iron oxides, quartz, and carbonate (Fig. 1 and Fig. 6) with sizes in the micron range. Quartz overgrowths are frequently observed in BST, and appear in a variety of shapes and sizes (Fig. 1 and Fig. 9), generally showing relatively flat surfaces. High-resolution SEM observations of uncoated quartz overgrowths confirm the presence of sub-micron particles of different sizes and shapes (from subhedral to blade-like).

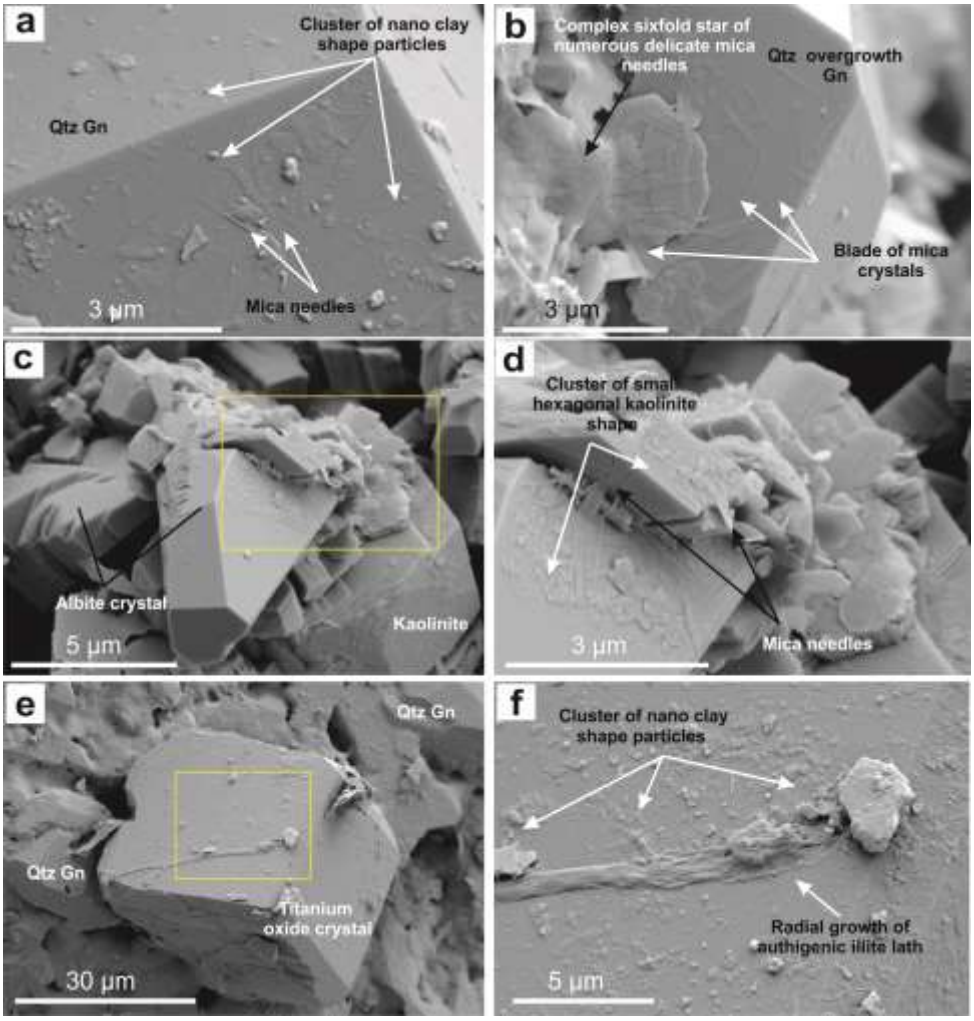

Figure 9. SEM micrographs showing different types of nanoparticles over detrital grains and clay minerals in BST. a) Electron micrograph of a quartz grain from the BST covered by numerous mica needles and clusters of nano-sized clay (lath-shaped). b) Electron micrograph of a hexagonal kaolinite crystal covered by numerous mica needles which extend over the underlying quartz overgrowth (BST.3). c) Electron micrograph of mica needles and clusters of nano-particles over albite and kaolinite crystals on BST.2. d) Enlargement of a part of albite crystal from (c) showing further details of the mica needles and a cluster of small hexagonal, nano-sized, kaolinite crystals. e) Electron photomicrograph of a truncated, octahedral, TiO_2 single crystal with exposed {001} and {101} facets lying on the detrital quartz grains which is coated with nano-sized clay crystals and authigenic illite (BST.4). f) Enlargement of the TiO_2 from (d) showing mica blades, and clusters of nano-sized clays, and authigenic illite laths collapsed on top of one another in a random manner. Qtz = quartz, and Gn= grain.

Figs 9a and 9b show examples of needle-shaped particles and nanometer sized kaolinite-like crystals on uncoated detrital quartz surfaces. Similar nanoscale objects are observed on the surface of feldspar and anatase crystals (Figs 9c and 9d). These observations align with the nanometer range needle-shaped minerals observed by Gary and Rex (1966), who used SEM and XRD to analyze the effluent from core flooding performed on BST, and postulated these to be mica crystals. Figs 9e and 9f show that these nanosized clay-shaped particles are probably forms of fibrous illite.

Nano-sized clay-shaped particles are of interest to the petroleum industry because these objects are challenging to characterize and may disproportionately affect hydrocarbon production (Gray and Rex, 1966; Stalder, 1973; Pallatt et al., 1984).To further characterize BST mineral surfaces with nanometer resolution, atomic force microscopy (AFM) was employed. AFM characterization revealed small particles (10 nm - 400 nm) over the studied mineral surfaces. Fig. 10 shows an SEM image of uncoated quartz overgrowth (BST.4 sample) and three AFM-PeakForce™ images taken at various positions on its surface. The AFM images show a multitude of small crystals, with different shapes, ranging from round to lath-like, and sizes up to ~ 400 nm. The subhedral shape of some of these crystals resembled some of the micro-crystals imaged using the SEM (Fig. 6) and are shown in Fig. 10c. In other cases, subhedral particles resembling kaolinite were also observed (Figs 10b and 10c). These type of crystals were also observed using SEM, as can be seen in Fig. 9b. In their study, Gray and Rex (1966) also identified kaolinite-shaped nanoparticles, which corroborate our observations. SEM and AFM results show that only the authigenic blade- or needle-shaped crystals are probably illite and only the smallest crystals of authigenic kaolinite are mobile and coat the surfaces of other minerals, such as quartz in the BST core specimens. This finding agrees with Gray and Rex's observation that dispersion of mica needles and small kaolinite crystals are the principal cause of clay mineral based fines migration. These authors also suggested that the nanoparticles adsorbed to mineral surfaces via the Coulombic attraction of doubly charged ions such as calcium.

3.3.2 Kaolinite surfaces. High-resolution SEM images show that the kaolinite basal planes are also covered by significant amounts of nanoparticles (Figs. 9b and 9d), the shape and sizes of these nanoparticles is the same as those observed in the quartz crystals and therefore are also identified as nanosized kaolinite and fibrous illite. The area occupied by these authigenic nano-particles could not be accurately measured, but as with quartz crystals surfaces, the presence of these minerals needs to be accounted for when assessing the reactivity of surfaces in contact with pore fluids. Compared to the other main clay minerals present in BST (illite/smectite and chlorite) kaolinite crystal crystals show mostly a well-developed, pseudo-hexagonal shape (Fig. 6) and, in most cases, it is the edge sites that are a the more exposed surface in the pore space, as opposed to the basal planes. This arrangement has important implications in terms of the oil retention capacity of the pore surfaces, as they are expected to be more reactive, and their reactivity pH dependent as well Nasralla and Nasr-

El- Din (2014). As described by Nasralla and Nasr- El- Din (2014), the pH dependence and ion sorption reactions within the edges can create a negative site (dominated by SI:Al-O^- edge sites) for the particle at reservoir conditions. These sites will coordinate to oppositely charge dangling bonds in the oil fraction (– $CooCa^+$, – NH^+) and any complexed salt ions occur and electrostatic bridges form, whose quantity determines the strength of oil adhesion to the kaolinite surface. The non-basal (i.e. non 00*l*) surfaces are very pH sensitive relative to the basal surfaces and may show rapid changes in structure as a function of EOR flood chemistry (Brady et al. 2012). Brady et al. (2012) highlighted their model on clay minerals, specifically kaolinite since its morphology permits a high concentration of unfulfilled bonds at sheet edges and corners, as well as natural impurities, which therefore generate a high chemical, surface reactivity that has been suggested to dominate enhanced oil recovery.

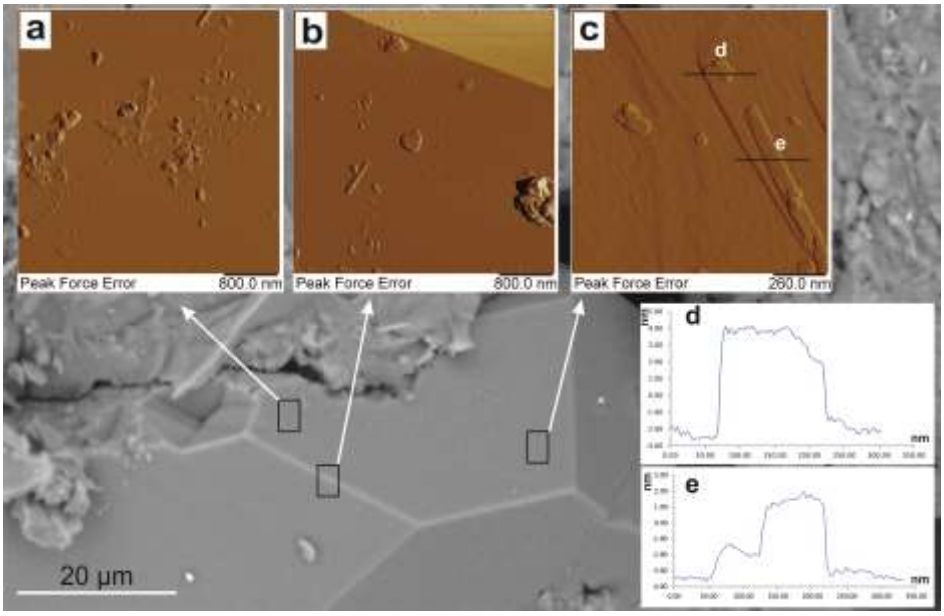

Figure 10. Background shows secondary electron photomicrographs of uncoated quartz overgrowth crystal from BST.4. a-c) AFM PeakForce™ images taken at the highlighted locations on the quartz surface showing nano-sized illite needles and a cluster of nano-sized hexagonal kaolinite-like crystals. d and e) show cross sections from nanoparticles in c).

3.4 Porosity characterization. To obtain a detailed understanding of the pore network of the four BST samples two complementary techniques were used µ-XCT and MICP. It is notable that µ-XCT and MICP approaches can generate different results in porosity (Peng et al. 2012). This is in part due to the fact that MICP can account for pore volumes that are accessible via pore throat sizes with equivalent diameters between 3nm and 360 nm, whereas micro-XCT can only account for a "modeled" pore space resolvable above the 1.03 micron resolution limit.

3.4.1 µ-XCT results. Analysis of the porosity by µ-XCT was carried out using the maximum resolution possible (1.03 µm) in a volume of 1 mm^3. The volume and number of pores were calculated for each BST specimen and are summarized in Table 5.

Table 5. Overall porosity, the share of pores and apparent porosity for the four BST samples studied, as determined by μ-XCT and MIP.

Sample No.	μ-XCT					MICP
	Overall porosity in the range >1 μm (%)	Share of pores within the range of pore size (% Vol):				Porosity (%)
		1 - 10μm	10 - 100μm	100 – 250 μm	250 - 500 μm	
BST.1	16.1	45	32	23	0	17.4
BST.2	18.6	35.5	11.4	48	5.1	19.3
BST.3	16.9	47	30	23	0	17.2
BST.4	23.6	23.6	22.2	58.1	9.9	21.2

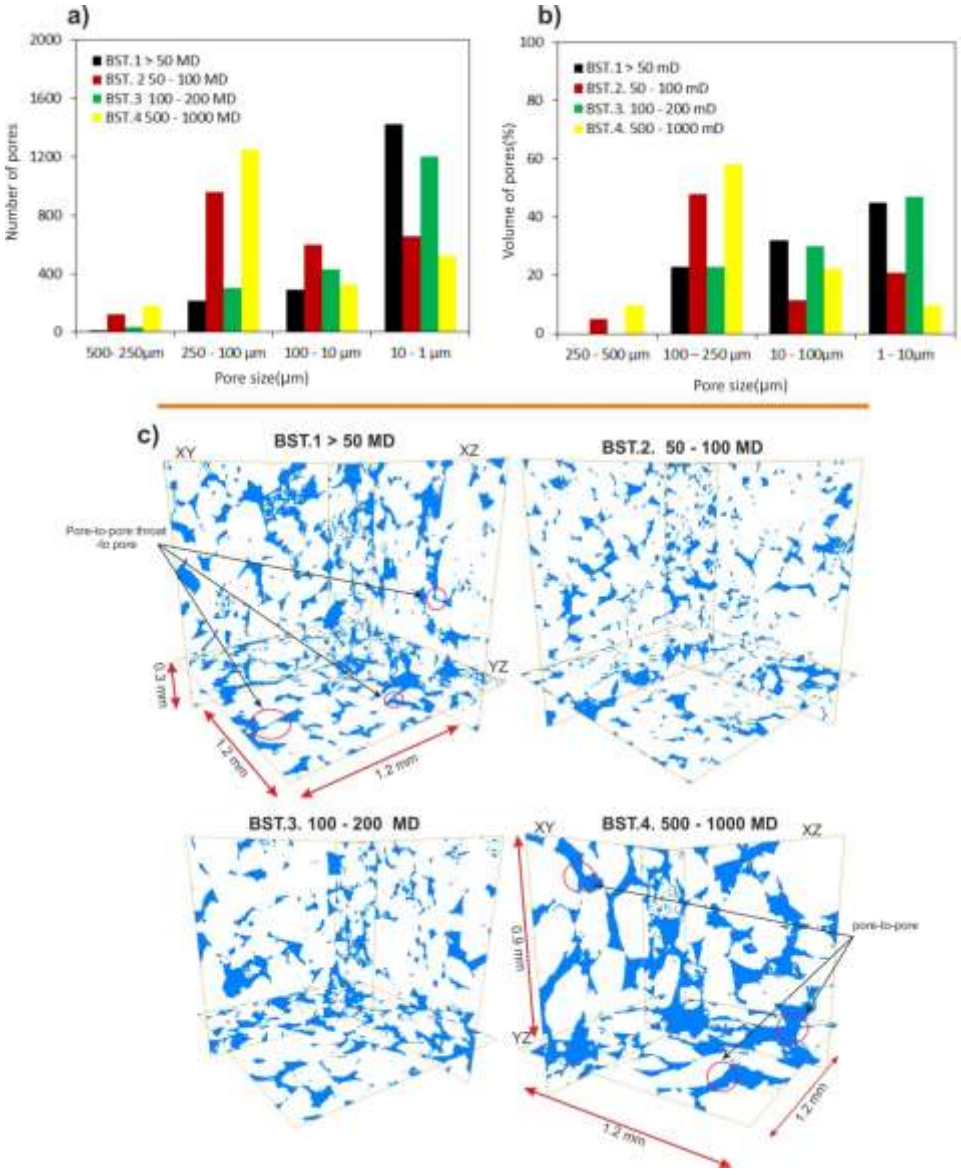

Figure 11. Porosity data obtained from analysis of μ-XCT data. a) Number of pores versus pore size fraction for the four BST samples studied. b) Volume of pores (%) versus pore size fraction. c) Three different cross-sectional views of the 3D reconstructed microstructure (at 100 slices), with XY, XZ and YZ sections at 1.2mm, 1.2mm and 1.2 mm, respectively.

As expected for sandstones dominated by primary intergranular pore systems, the permeability of BST samples increases with porosity (Table 5), as measured by micro-XCT. However this overall increase does not follow a linear trend and whereas the measured porosity (from μ-XCT measurements) increased from 16.1% to 18.6% for the BST.1 samples and BST.2 samples, respectively, it decreased to 16.9% for BST.3 samples and increased again to 23.6 % for BST.4 samples. Fig. 11 shows the results from the quantification of the number and volume of pores within 4 pore size fractions (1-10 μm, 10-100 μm, 100-250 μm and 250-500 μm). Fig. 11a shows most of the pores in the 4 sample sets have a size smaller than 100 μm. However, when the volume fraction of each sample is taken into account the relevance of the large pore fraction (> 100 μm) in the total porosity becomes clearer. Based on this, samples in the 4 BST permeability groups can be grouped into two categories, for samples BST.1 and BST.3 pores with a size larger than 100 μm represent just above 20% of the pore volume, whereas for samples BST.2 and BST.4 they represent more than 60% of the pore volume. Examples of the final 3D binary images showing the pore volume fraction for the four BST samples analysed are shown in Fig. 11c. Additionally, results obtained from the analysis of BST.4 samples align well with the findings of the work of Berg et al. (2014), where an average permeability of 700 mD and a porosity of 19.9% were determined for 6 different BST core plugs. Furthermore, Leu et al. (2014) found that segmentation methods in BST core samples lead to different results for the computed physical properties such as porosity. The computed results in this study closely match with experimental values in the work of Peng et al. (2012), where MICP was used to determine a total porosity in the bulk sample without an epoxy coating of 23.2% based on the bulk density (2.03 g/cm^3).

Results from BST cores shows that the number of pores decreases exponentially as the pore-volume increases further. This is in agreement with the work of Bera et al. (2011) on BST, who found similar results in their FIB–SEM data, showing it is important to understand pore connectivity and the percolating network. Fig 11c furthermore shows that vuggy/moldic-like shapes (of size ≥ 200 μm) in BST.1 are connected through the edge of pore bodies (of size ~200 μm) and not directly to other vuggy/moldic-like body shapes. In contrast, it is seen that vuggy/moldic-like shapes are connected directly to other pore bodies in BST.2, BST.3 and BST.4 samples.

3.4.2 Pore network connectivity. Porosity was estimated by micro-XCT models and MICP using the same representative samples of each BST group. MICP porosity measurement results are shown in Table 5. In this work, MICP porosity results are typically 10% lower than porosity results obtained by micro-XCT. The difference in value is related to micro-XCT analysis since total porosity is including both accessible and isolated pores (Peng et al. 2012). The fact that the values are so comparable stems, in part, from using the highest resolution scan mode in the μ-XCT. It is clear that results show the same trend on porosity variation with respect to sample porosity as was measured with the μ-

XCT. To gain a deeper understanding of the pore structure and connectivity across samples, a detailed high-resolution SEM study was undertaken. Fig. 12 shows results from the mercury injection experiments for the four groups of samples (BST.1 – BST.4). From this figure, it can be clearly seen that BST.2 and BST.3 have a bimodal pore throat distribution, as opposed to the BST.1 and BST.4 samples, which show an unimodal distribution. Therefore, once again the results allowed grouping of the 4 sample sets into two categories. For BST.2 and BST.3the first peak (pore throat size) has its maximum between 0.1and 0.3µm correspond to (1P) and (1T), whereas the second peak (pore throat size) is, in both groups, located above 0.5µm, and up to 200µm correspond to (2p) and (2T). These samples encompass the two intermediate permeability values. In contrast, for BST.1 and BST.4 group of selected samples an unimodal distribution of pore throat sizes was only observed, the large (1k) peak in BST.1 corresponding to pore throat sizes between 0.5µm to 200µm. Although the large peak (1s) in BST.4 is also identified, the pore throat sizes are located between 0.5 µm to 500 µm as shown in Fig.12.

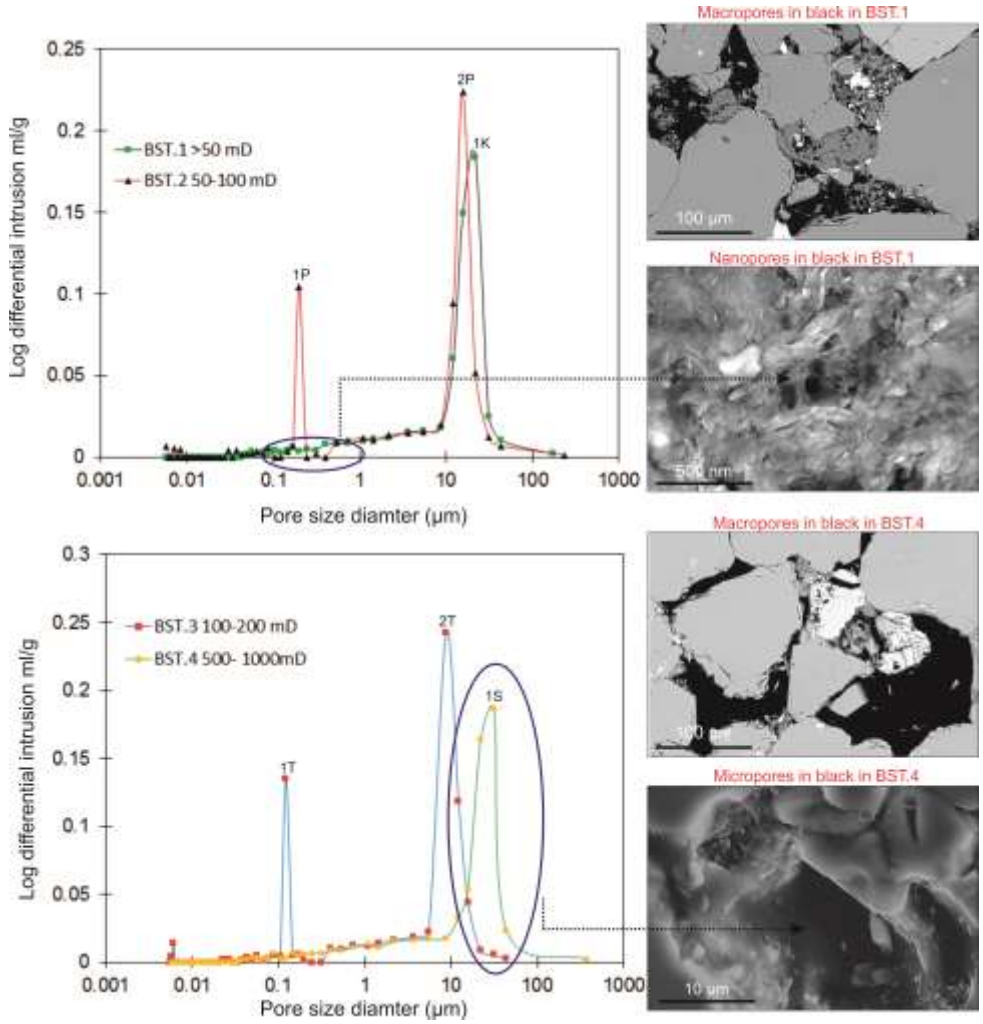

Figure 12. Mercury injection versus pore size curves for samples BST.1/2 (a) and BST.3/4 (b). SEM images show the different pore throat types associated to each peak in the curves.

Despite the difference in permeabilities in the case of BST.1 and BST.4, both low and high permeability ranges exhibit unimodal and relatively larger pore throat sizes than those found in BST.2 and BST.3 samples. It is clear the MICP data for selected BST core sample reflect the entire pore throat. In addition to MIP and -XCT additional SEM observations were carried out to fully characterize the pore network and connectivity down to the nanometer scale, and therefore obtain a complete picture to link porosity to permeability. High-resolution SEM images indicate that the pores observed in equivalent samples can be assigned into two groups: inter-grain (pores along quartz contacts) and intra-grain (Figs. 13a and 13c). Small size pores (< 1μm) mostly exist within the clay mineral matrix, which, in the case of samples from BST.1, BST.3, and BST.4 consists mostly of kaolinite compared to illite for BST.2 (Figs.13e and 13f). Neasham (1977) proposed that the distribution of clay morphologies significantly affected sandstone porosity-permeability relationships, postulating that patchy discrete clay particles (e.g. kaolinite booklet-like micro aggregates) have less effect on fluid flow than clays lining the entire pore or congesting pore throats. As the degree of internal porosity of these kaolinite aggregates is smaller than that of the illite coatings (Fig. 13c), this may explain the larger number of small-size pores observed by μ-XCT (Fig. 11) in BST.1 and BST.3.

SEM observations suggest that kaolinite aggregates could be one of the factors which are responsible for the permeability reduction in BST.1 compared with the rest of the BST samples, as the crystals are of relatively large size compared to the pore size and also appear to be only loosely attached to detrital grains. Fig.13e shows kaolinite-blocked cavities between detrital grains. This characteristic helps explain the MICP data for BST.1 samples, which suggested that the pore throats are not well connected (which will decrease overall permeability). In comparison to BST.1 samples, analysis of clay minerals in the BST.2 samples show illite to dominate the larger fractions.

Based on the SEM analysis, pore throats in illite aglomerates, which form the pathways in the pore network in BST.2 samples, tend to be more exposed to the open pore space. Examples of illite coatings are shown in Figs.13i. Due to the fibrous nature of illite, many pore throats within the illite matrix will be connected to the open main pore space. Intuitively, it might be expected that the BST.2 samples, with more authigenic fibrous illite, would have a greater loss of permeability, however, the results indicate that authigenic kaolinite in BST.1 samples reduces permeability more when compared with the BST.2 samples. This is in contrast to the analysis by Neasham (1977), who suggested that authigenic kaolinite filled pores would have the least effect on transport properties. In addition, clay minerals in the BST.3 samples show illite fractions in the scanned area are more dispersed between detrital grains when compared with BST.4 samples. This could be one of the main reasons that the small pore throats in BST.3 samples are exposed to the open pore spaces, as can be seen in (Fig.12).This indicates that the illite pore-lining clays in the BST.3 samples have the most effect on pore network properties. However, the high fraction of kaolinite shown by EDX in the BST.4 sample, suggests that it is unlikely that they contribute greatly to permeability reduction.

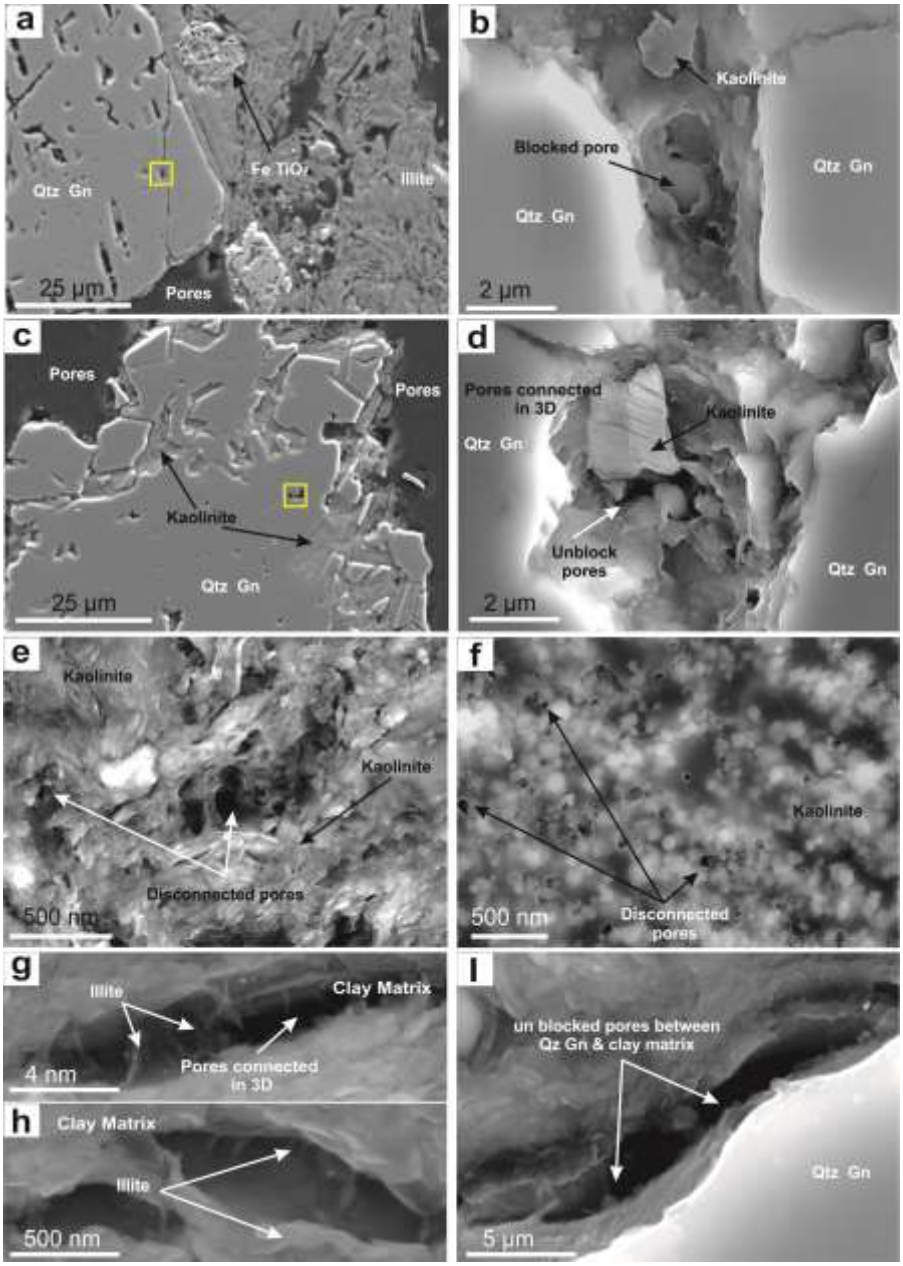

Figure 13. SEM and BSE micrographs showing the variation of pore distribution and pore connectivity in the BST cores studied: a) Example of intra-grain porosity in the detrital quartz grains in BST.1, as well as the porous framework of illite aggregates. b) Zoomed in, isolated pore (from (yellow box in a)). The pores in centre of the image are blocked by kaolinite which can significantly affect to overall porosity. c) BSE micrograph showing the kaolinite aggregates between detrital quartz grains in BST.2, which display a smaller internal porosity than illite agglomerates. d) Enlargement from yellow box in (c) showing pore lining kaolinite. e and f) High resolution images showing pore lining kaolinite in BST.1 and BST.3, respectively. Smaller pores in the aggregates show no sign of 3-D connectivity. g), and h), High resolution images from BST.3 showing elongated pores embedded with illite crystals. These pores are framed by fibrous illite minerals that allows for connectivity along the pore. i). High resolution images from BST.2

Results from the characterization show that the pore network in BST.1 is not well connected as the majority of clay minerals exposed to pore space are kaolinite, down to the resolution of the SEM (Fig. 12). Along with the pore connectivity in the clay mineral matrix, microstructural observations identify most of the pore throats as intra-grain which form the pathways in the pore network, and these are also blocked at and below the resolution of the SEM (i.e. < 2 μm width, Fig. 13b). The μ-XCT data identifies the heterogeneity in geometry in the pore network in BST.1 samples compared to other BST core plugs, as discussed in Section 3.4.1. This reveals that the permeability in BST.1 samples is mainly controlled by the pore connectivity in the clay mineral matrix, in intra-grain pores, as well as the geometry of the porous network. In contrast, analyses suggest that the clay mineral matrix is mostly connected to pore spaces in BST.2 and BST.3 samples (Fig.12).

When attempting to link intra-grain throats to permeability, it is important to know the connectivity of intra-grain pores (e.g. in quartz detrital grains). The observations from SEM images shows that the intra-grain pore throats are connected and have not been blocked by clay minerals such as kaolinite (see fig.13d) owing to the larger pore-throat sizes being more abundant in BST.2, 3, and 4 samples compared with BST.1 samples. Comparing the computed geometry of the porous network in the BST cores studied, the pores in BST.2, BST.3 and BST.4 samples are often in direct contact with another pore through the body rather than at the edges of pores, as can be seen in (Fig.11). These results also offer an explanation as to why there is an increase in permeability within the studied samples.

EOR can partially be explained by permeability reduction in the water swept zone, due to fines migration when low salinity water brine is injected (Tang and Morrow, 1999; Lager et al., 2006). Recently, it has been observed that increased oil recovery could be the result of improved microscopic sweep efficiency rather than the wettability alteration processes (Li, 2008; Skauge et al., 2008). In fact, Tang and Morrow (1999) performed EOR experiments on Berea core sandstone and concluded that the fine (particle) mobilization (mainly kaolinite) increased oil recovery. In that sense, it is essential for a successful low salinity project to understand not only the morphology and identity of the main clay minerals in the samples studied but also their distribution with respect to the pore network, and in particular to pore throats. In the case of BST, that will be the case of either illite or kaolinite.

4. Conclusions

Berea core sandstone is widely used by industry as a proxy for one of the principal oil-bearing rocks. Therefore the characterization of its composition, pore structure and the distribution of minerals within the connected pore network is crucial for recovery correct analysis of core-flood experiments related to EOR, fine migrations or other type of studies. In this paper, a wide range of techniques were used to characterize 4 types of samples of BST at scales ranging from nanometer to millimeter in order to address the pore surface chemistry as well as the heterogeneity in the mineral and pore sizes distribution. Differences in these parameters will determine the types and quantities of mineral surfaces accessible to react with oil, brine or other fluids and therefore will determine the type of response of Berea sandstone in coreflood experiments. The main conclusions of our characterisation study are:

1. The volumetric compositions of the selected BST are dominated (>87 %) by detrital quartz and K-feldspar. In terms of clay minerals, the volumetric fraction of each of the main clay types (kaolinite, illite/smectite, and chlorite) varied across the 4 different permeability ranges studied (from 3.4 to 9.1 %). This translates into a different amount of clay minerals contained within the total pore space. More importantly, perhaps, is the fact that the identity of the clay minerals exposed to the open pore space is different across the studied specimens.
2. Nano-sized clay-like crystals were observed over most quartz grains surfaces and on larger clay minerals such as kaolinite basal surfaces within the BST core specimens. Their origin, crystallography, chemical reactivity and surface-bonding relationships are in need of further study and future EOR experiments are ongoing to shed light on the importance of these nano-scale particles for reservoir management.
3. Carbonate cement is present, though localized in the BST. Silica cement is also prevalent in all of the BST specimens, including both as crystalline quartz and amorphous silica.
4. Porosity shows a positive, albeit non-linear, correlation with permeability across the BST cores studied. The permeability of the all BST core samples is mainly controlled by the pore connectivity within both the clay matrix and authigenic clays. Next to pore connectivity, pore morphology is also important, especially when the large pores are connected through relatively smaller pores or edges, without being connected directly to the body of the pore.

Results from this work show that Berea sandstone cores can show significant variability and heterogeneity at both microscopic and nanoscopic scales, which undoubtedly will play a role in determining the rock's interaction with a fluid (being oil, brine or other solution). Performing a full "multi-scale" characterisation, therefore, will be critical in the planning, execution and analysis of core flood experiments in the lab.

Acknowledgements

This work was supported by the Kurdistan Regional Government (KRG). The research was also partially supported by BP, and we thank Dr. Ian Collins and Dr. Peter Salino for many useful discussions. HCG acknowledges the Royal Society for funding via an Industry Fellowship. Finally, we also want to thank Philip Green at the University of Newcastle for mercury porosimetry, and Ian Chaplin (Durham University, Earth Sciences Department) for preparing and making a thin section, polish thin section, and polished resin. SH acknowledges the support of the Rural & Environment Science & Analytical Services Division of the Scottish Government.

References

1. Abell, A.B., Willis, K.L., Lange, D.A., 1998. Mercury intrusion porosimetry and image analysis of cement-base materials. Journal of Colloid and Interface Science 211, 39–44.
2. Aghaeifar, Z., Strand, S., Austad, T., Puntervold, T., Aksulu, H., Navratil, K., & Håmsø, D. (2015). Influence of Formation Water Salinity/Composition on the Low-Salinity Enhanced Oil Recovery Effect in High-Temperature Sandstone Reservoirs. Energy & Fuels, 29(8), 4747-4754.
3. Alotaibi, M. B., Nasralla, R. A., & Nasr-El-Din, H. A. (2011). Wettability studies using low-salinity water in sandstone reservoirs. SPE Reservoir Evaluation & Engineering, 14(06), 713-725.
4. Al-Ramadan, K., Morad, S., Proust, J. N., & Al-Aasm, I. (2005). Distribution of diagenetic alterations in siliciclastic shoreface deposits within a sequence stratigraphic framework: evidence from the Upper Jurassic, Boulonnais, and NW France. Journal of Sedimentary Research, 75(5), 943-959.
5. Alvarado, V., & Manrique, E. (2010). Enhanced oil recovery: an update review. *Energies* **3**, 1529-1575.
6. Balthazor, D.A., 1991, Sedimentology of the Bedford-Berea sequence (Early Mississippian), Williams Field, Michigan: Kalamazoo, Western Michigan University, Master's Thesis, 144 p.
7. Baraka-Lokmane, S., Main, I. G., Ngwenya, B. T., & Elphick, S. C. (2009). Application of complementary methods for more robust characterization of sandstone cores. Marine and Petroleum Geology, 26(1), 39-56.
8. Baveye, P. C., Laba, M., Otten, W., Bouckaert, L., Sterpaio, P. D., Goswami, R. R., & Sezgin, M. (2010). Observer-dependent variability of the thresholding step in the quantitative analysis of soil images and X-ray microtomography data. Geoderma, 157(1), 51-63.
9. Beaufort, D., Cassagnabere, A., Petit, S., Lanson, B., Berger, G., Lacharpagne, J. C., & Johansen, H. (1998). Kaolinite-to-dickite reaction in sandstone reservoirs. Clay Minerals, 33(2), 297-316.
10. Bera, B., Mitra, S. K., & Vick, D. (2010). Understanding the micro structure of Berea Sandstone by the simultaneous use of micro-computed tomography (micro-CT) and focused ion beam-scanning electron microscopy (FIB-SEM).Micron, 42(5), 412-418.
11. Bera, B., Mitra, S. K., & Vick, D. (2011). Understanding the micro structure of Berea Sandstone by the simultaneous use of micro-computed tomography (micro-CT) and focused ion beam-scanning electron microscopy (FIB-SEM).Micron, 42(5), 412-418.

12. Berg, S., Armstrong, R., Ott, H., Georgiadis, A., Klapp, S. A., Schwing, A., ... & Enzmann, F. (2014). Multiphase flow in porous rock imaged under dynamic flow conditions with fast X-ray computed microtomography. Petrophysics, 55(04), 304-312.
13. Bjorlykke, K. 1998. 'Clay Mineral Diagenesis in Sedimentary Basins; a Key to the Prediction of Rock Properties; Examples from the North Sea Basin'. Clay Minerals 33 (1): 15–34. http://claymin.geoscienceworld.org/content/33/1/15.
14. Brady, P. V., & Krumhansl, J. L. (2012). A surface complexation model of oil–brine–sandstone interfaces at 100° C: Low salinity waterflooding. Journal of Petroleum Science and Engineering, 81, 171-176.
15. Buades, A., Coll, B., & Morel, J. M. (2005). A non-local algorithm for image denoising. In Computer Vision and Pattern Recognition, 2005. CVPR 2005. IEEE Computer Society Conference on (Vol. 2, pp. 60-65). IEEE.
16. Buchwalter, E., Swift, A.M., Sheets, J.M., Cole, D.R., Prisk, T., Anovitz, L.L., Ilavsky, J., Rivers, M., Welch, S. and Chipera, D., 2015. Mapping of Microbial Habitats in Organic-Rich Shale. Unconventional Resources Technology Conference (URTEC).
17. Churcher, P. L., French, P. R., Shaw, J. C., & Schramm, L. L. (1991). Rock properties of Berea sandstone, Baker dolomite, and Indiana limestone. In SPE International Symposium on Oilfield Chemistry. Society of Petroleum Engineers.
18. Civan, F. (2011). Reservoir formation damage. Gulf Professional Publishing.
19. Cnudde, V., Cwirzen, A., Masschaele, B., & Jacobs, P. J. S. (2009). Porosity and microstructure characterization of building stones and concretes. Engineering geology, 103(3), 76-83.
20. Dawson, G. K. W., Pearce, J. K., Biddle, D., & Golding, S. D. (2015). Experimental mineral dissolution in Berea Sandstone reacted with CO_2 or SO_2–CO_2 in NaCl brine under CO_2 sequestration conditions. Chemical Geology, 399, 87-97.
21. Dilks, A., & Graham, S. C. (1985). Quantitative mineralogical characterization of sandstones by back-scattered electron image analysis. Journal of Sedimentary Research, 55(3).
22. El-Ghali, M.A.K., Mansurbeg, H., Morad, S., Al-Aasm, I., Ajdanlisky, G., 2006b. Distribution of diagenetic alterations in fluvial and paralic deposits within sequence stratigraphic framework: evidence from the Petrohan terrigenous group and the svidol formation, lower Triassic, NW Bulgaria. Sedimentary Geology 190, 299e321.
23. Folk, R.L., (1980). Petrology of Sedimentary Rocks. Hemphill Publ. Co., Austin. 182 pp.
24. Garnes, W. T. (2014). Subsurface Facies Analysis of the Devonian Berea Sandstone in Southeastern Ohio (Doctoral dissertation, Bowling Green State University).
25. Gautier, J. M., Oelkers, E. H., & Schott, J. (2001). Are quartz dissolution rates proportional to BET surface areas?. Geochimica et Cosmochimica Acta, 65(7), 1059-1070.
26. Golab, A., Romeyn, R., Averdunk, H., Knackstedt, M., & Senden, T. J. (2013). 3D characterisation of potential CO_2 reservoir and seal rocks. Australian Journal of Earth Sciences, 60(1), 111-123.
27. Gray, D. H., & Rex, R. W. (1966). Formation damage in sandstones caused by clay dispersion and migration. In Proc (pp. 355-365). Clays and Clay Minerals 1966 14: 355-366.
28. Hassenkam, T., Pedersen, C. S., Dalby, K., Austad, T., & Stipp, S. L. S. (2011). Pore scale observation of low salinity effects on outcrop and oil reservoir sandstone. Colloids and Surfaces A: Physicochemical and Engineering Aspects, 390(1), 179-188.
29. Hezel, D. C., Elangovan, P., Viehmann, S., Howard, L., Abel, R. L., & Armstrong, R. (2013). Visualisation and quantification of CV chondrite petrography using micro-tomography. Geochimica et Cosmochimica Acta, 116, 33-40.
30. Hildenbrand, A., Urai, J.L., 2003. Investigation of the morphology of pore space in mudstones - first results. Marine Petroleum Geology 20, 1185–1200.
31. Houston, A. N., Schmidt, S., Tarquis, A. M., Otten, W., Baveye, P. C., & Hapca, S. M. (2013). Effect of scanning and image reconstruction settings in X-ray computed microtomography on quality and segmentation of 3D soil images. Geoderma, 207, 154-165.

32. Howard, J.J., 1991. Porosimetry measurement of shale fabric and its relationship to illite/smectite diagenesis. Clays and Clay Minerals 39 (3), 355–361.
33. Hurst, A. (1999).Textural and geochemical micro-analysis in the interpretation of clay mineral characteristics; lessons from sandstone hydrocarbon reservoirs. Clay Minerals, 34(1), 137-149.
34. Kilda, L., & Friis, H. (2002).The key factors controlling reservoir quality of the Middle Cambrian Deimena Group sandstone in West Lithuania. Bulletin of the Geological Society of Denmark, 49(1), 25-39.
35. Lager, A., Webb, K. J., Collins, I. R., & Richmond, D. M. (2008). LoSal enhanced oil recovery: Evidence of enhanced oil recovery at the reservoir scale. In SPE Symposium on Improved Oil Recovery. Society of Petroleum Engineers.
36. Lager, A., Webb, K.J. and Black, C.J.J., 2006. Impact of brine chemistry on oil recovery, Paper A24 presented at the 14th European Symposium on Improved Oil Recovery, Cairo, Egypt.
37. Lai, P., & Krevor, S. (2014). Pore scale heterogeneity in the mineral distribution and surface area of Berea sandstone. Energy Procedia, 63, 3582-3588.
38. Lai, P., Moulton, K., & Krevor, S. (2015). Pore-scale heterogeneity in the mineral distribution and reactive surface area of porous rocks. Chemical Geology, 411, 260-273.
39. Landrot, G., Ajo-Franklin, J. B., Yang, L., Cabrini, S., & Steefel, C. I. (2012). Measurement of accessible reactive surface area in a sandstone, with application to CO_2 mineralization. Chemical Geology, 318, 113-125.
40. Laškova L.N., 1987, The Cambrian: Oil fields of the Baltic region: Vilnius Mokslas p. 10–22 (in Russian)
41. Lebedeva, E. V., Fogden, A., Senden, T. J.,& Knackstedt, M. A.(2010). Kaolinite Wettability— The Effect of Salinity, pH and Calcium ,Society of Core Analysts.
42. Lebedeva, E.V.,&Fogden, A(2011). Wettability alteration of kaolinite exposed to crude oil in salt solutions. Colloids and Surfaces A: physicochemical and Engineering Aspects, 377(1), 115-122.
43. Lee, S. Y., Webb, K. J., Collins, I. R., Lager, A., Clarke, S. M., O'Sullivan, M., & Routh, A. F. (2011, April). Low Salinity Oil Recovery–Increasing Understanding of the Underlying Mechanisms of Double Layer Expansion. In IOR 2011.
44. Lee, S. Y., Webb, K. J., Collins, I., Lager, A., Clarke, S., O'Sullivan, M., & Wang, X. (2010, January). Low salinity oil recovery: Increasing understanding of the underlying mechanisms. In SPE Improved Oil Recovery Symposium. Society of Petroleum Engineers.
45. Leu, L., S. Berg, F. Enzmann, R. T. Armstrong, and M. Kersten. 2014. 'Fast X-Ray Micro-Tomography of Multiphase Flow in Berea Sandstone: A Sensitivity Study on Image Processing'. Transport in Porous Media 105 (2): 451–69. doi:10.1007/s11242-014-0378-4
46. Li, M., Linked polymer solution (LPS) and its application in EOR. The 29th IEA Workshop & Symposium, Beijing, China, Nov 3-5, 2008
47. Marle, C. M. (1991). Oil entrapment and mobilization. Basic Concepts in Enhanced Oil Recovery Processes, M. Baviere, Eds. Elsevier Applied Science, 3-39.
48. Matthiesen, J., Bovet, N., Hilner, E., Andersson, M. P., Schmidt, D. A., Webb, K. J.,& Stipp, S. L. S. (2014). How naturally adsorbed material on minerals affects low salinity enhanced oil recovery. Energy & Fuels, 28(8), 4849-4858.
49. Metz, V., Raanan, H., Pieper, H., Bosbach, D., & Ganor, J. (2005). Towards the establishment of a reliable proxy for the reactive surface area of smectite.Geochimica et Cosmochimica Acta, 69(10), 2581-2591.
50. Milliken, K. L., & Laubach, S. E. (2000). Brittle deformation in sandstone diagenesis as revealed by scanned Cathodoluminescence imaging with application to characterization of fractured reservoirs. In Cathodoluminescence in geosciences (pp. 225-243). Springer Berlin Heidelberg.

51. Morrow, N. R., Tang, G. Q., Valat, M., & Xie, X. (1998). Prospects of improved oil recovery related to wettability and brine composition. Journal of Petroleum science and Engineering, 20(3), 267-276.
52. Nasralla, R. A., Alotaibi, M. B., & Nasr-El-Din, H. A. (2011, January). Efficiency of oil recovery by low salinity water flooding in sandstone reservoirs. In SPE Western North American Region Meeting. Society of Petroleum Engineers
53. Neasham, J. W. (1977, January). The morphology of dispersed clay in sandstone reservoirs and its effect on sandstone shaliness, pore space and fluid flow properties. In SPE Annual Fall Technical Conference and Exhibition. Society of Petroleum Engineers.
54. Omotoso, O., McCarty, D. K., Hillier, S., & Kleeberg, R. (2006). Some successful approaches to quantitative mineral analysis as revealed by the 3rd Reynolds Cup contest. Clays and Clay Minerals, 54(6), 748-760.
55. Otten, W., Pajor, R., Schmidt, S., Baveye, P. C., Hague, R., & Falconer, R. E. (2012). Combining X-ray CT and 3D printing technology to produce microcosms with replicable, complex pore geometries. Soil Biology and Biochemistry, 51, 53-55.
56. Pallatt, N., Wilson, J., & McHardy, B. (1984). The relationship between permeability and the morphology of diagenetic illite in reservoir rocks. Journal of Petroleum Technology, 36(12), 2-225.
57. Peng, S., Hu, Q., Dultz, S., & Zhang, M. (2012). Using X-ray computed tomography in pore structure characterization for a Berea sandstone: resolution effect. Journal of Hydrology, 472, 254-261.
58. Pepper, J. F. et al. (1944) Map of the Second Berea sand in Gallia, Meigs, Athens, Morgan, and Muskingum Counties, Ohio, U. S. Geol. Survey, Oil and Gas Invest., Prelim, map no. 5
59. Pepper, J. F.; DeWitt, W.; and Demarest, D. F., 1954, Geology of the Bedford shale and Berea sandstone in the Appalachian Basin: U.S. Geol. Survey Prof. Paper 259, 111 p.
60. Peters, C. A. (2009). Accessibilities of reactive minerals in consolidated sedimentary rock: An imaging study of three sandstones. Chemical Geology, 265(1), 198-208.
61. Scholle, D., & Scholle, P. (n.d.). , (2014) A Color Guide to the Petrography of Sandstones, Siltstones, Shales and Associated Rocks.
62. Skauge, A.; Fallah, S.; McKay, E., Modeling of LPS Linked Polymer Solutions. The 29th IEA Workshop & Symposium, Beijing, China, Nov 3-5, 2008.
63. Soeder, D. J. (1986). Laboratory drying procedures and the permeability of tight sandstone core. SPE Formation Evaluation, 1(01), 16-22.
64. Sorbie, K. S., & Collins, I. (2010, January). A proposed pore-scale mechanism for how low salinity waterflooding works. In SPE Improved Oil Recovery Symposium. Society of Petroleum Engineers.
65. Stalder, P.J., 1973. Influence of crystallographic habit and aggregate structure of clay mineral on sandstone permeability. Geol. Mijnbouw, 52(4): 217--220.
66. Strand, Skule, Tor Austad, Tina Puntervold, Hakan Aksulu, Bjarne Haaland, and Alireza RezaeiDoust. 2014. 'Impact of Plagioclase on the Low Salinity EOR-Effect in Sandstone'. Energy & Fuels 28 (4): 2378–83. doi:10.1021/ef4024383
67. Tang, G.-Q, N. R. Morrow (1999). "Influence of brine composition and fines migration on crude oil/brine/rock interactions and oil recovery." Journal of Petroleum Science and Engineering 24(2–4): 99-111.
68. Tovey, N. K., & Krinsley, D. H. (1991). Mineralogical mapping of scanning electron micrographs. Sedimentary Geology, 75(1), 109-123.
69. Vosylius, G. (1998). Reservoir properties of Middle Cambrian rocks. In Proceedings of the International Scientific Conference "Prospectives of petroleum exploration in the Baltic Region". Lithuanian Geological Institute (pp. 43-48).

70. Waldmann, S., Busch, A., van Ojik, K., & Gaupp, R. (2014). Importance of mineral surface areas in Rotliegend sandstones for modeling CO_2–water–rock interactions. Chemical Geology, 378, 89-109.
71. Webb, K.J., C.J.J. Black, and I.J. Edmonds. Low salinity oil recovery - the role of reservoir condition core floods. in EAGE(Marle 1991) conference. 2005. Budapest, Hungary.
72. Wilson, M. D., & Pittman, E. D. (1977). Authigenic clays in sandstones: recognition and influence on reservoir properties and paleoenvironmental analysis. Journal of Sedimentary Research, 47(1).
73. Worden, R. H., French, M. W., & Mariani, E. (2012). Amorphous silica nanofilms result in growth of misoriented microcrystalline quartz cement maintaining porosity in deeply buried sandstones. Geology, 40(2), 179-182.
74. Yven, B., Sammartino, S., Geraud, Y., Homand, F., Villieras, F., 2007. Mineralogy, texture and porosity of Callovo-Oxfordian argillites of the Meuse/Haute-Marne region (eastern Paris Basin). Mémoires: Société Géologique de France 178, 73–90.
75. Zhang, F., She, Y. H., Li, H. M., Zhang, X. T., Shu, F. C., Wang, Z. L.& Hou, D. J. (2012). Impact of an indigenous microbial enhanced oil recovery field trial on microbial community structure in a high pour-point oil reservoir. Applied microbiology and biotechnology, 95(3), 811-821.
76. Zhang, P., Lee, Y. I., & Zhang, J. (2015). Diagenesis of tight-gas sandstones in the lower cretaceous denglouku formation, songliao basin, ne china: implications for reservoir quality. Journal of Petroleum Geology, 38(1), 99-114.